REPUBLIC OF TURKEY
ADANA ALPARSLAN TÜRKEŞ SCIENCE AND TECHNOLOGY UNIVERSITY

GRADUATE SCHOOL OF NATURAL AND APPLIED SCIENCES
DEPARTMENT OF ELECTRICAL - ELECTRONICS ENGINEERING

DESIGN AND CHARACTERIZATION OF A SINGLE LAYER UNCOOLED MICROBOLOMETER DETECTOR PIXEL

ÇİĞDEM YILDIZAK
MASTER OF SCIENCE

ADANA 2019

REPUBLIC OF TURKEY

ADANA ALPARSLAN TÜRKEŞ SCIENCE AND TECHNOLOGY UNIVERSITY

GRADUATE SCHOOL OF NATURAL AND APPLIED SCIENCES

DEPARTMENT OF ELECTRICAL - ELECTRONICS ENGINEERING

DESIGN AND CHARACTERIZATION OF A SINGLE LAYER UNCOOLED MICROBOLOMETER DETECTOR PIXEL

ÇİĞDEM YILDIZAK

MASTER OF SCIENCE

SUPERVISOR

Assoc. Prof. Dr. M. YUSUF TANRIKULU

ADANA 2019

DESIGN AND CHARACTERIZATION OF A SINGLE LAYER UNCOOLED MICROBOLOMETER DETECTOR PIXEL

submitted by **Çiğdem YILDIZAK** in partial fulfillment of the requirements for the degree of **Master of Science in Department of Electrical - Electronics Engineering, Adana Alparslan Türkeş Science and Technology University** by,

Assoc. Prof. Dr. Gözde BAYDEMİR PEŞİNT
Graduate School Director

Assoc. Prof. Dr. Mahmud Yusuf TANRIKULU
Department Chair

Assoc. Prof. Dr. Mahmud Yusuf TANRIKULU
Supervisor

Thesis Committee

Assoc. Prof. Dr. Mahmud Yusuf TANRIKULU
Adana Alparslan Türkeş Science and Technology University

Assist. Prof. Dr. Amira TANDİROVİÇ GÜRSEL
Adana Alparslan Türkeş Science and Technology University

Prof. Dr. Mutlu AVCI
Çukurova University

Thesis Defense Date

24/06/2019

1 hereby declare that ali informıation in this thesis has been obtained and presented in accordance with academic nıles and ethical conduct. 1 also declare that, as required by these rules and conduct, 1 have fully cited and referenced ali information that is not original to this work.

Çiğdem YILDIZAK

ABSTRACT

DESIGN AND CHARACTERIZATION OF A SINGLE LAYER UNCOOLED MICROBOLOMETER DETECTOR PIXEL

Çiğdem YILDIZAK
Department of Electrical - Electronics Engineering
Supervisor: Assoc. Prof. Dr. M. Yusuf TANRIKULU
June 2019, 76 pages
In this thesis, fabrication and characterization of a single layer uncooled microbolometer detector are presented. The single layer structure is developed to use the same material as the active material, the structural layer, and the absorber layer, and it is aimed to reveal a cost-effective solution for microbolometer type thermal detectors by decreasing the fabrication complexity.

The design starts with the determination of the single layer as Zinc Oxide (ZnO) which is coated with atomic layer deposition technique. Structural design of a single layer microbolometer detector pixel is performed by optimizing the design parameters with the optical, thermal, and mechanical simulations. The short and long-armed pixels are designed with the pitch values of 25, 35, and 50 µm; the ZnO thickness and the cavity thickness values of the designed pixels are optimized to have an absorption amount higher than 85% in the wavelength range of 8-12 µm. The thermal conductance values of the designed pixels are simulated in the range of $5x10^{-7}$ and $7.7x10^{-6}$ W/K while their thermal time constant values are simulated between 0.2 and 2.8 ms.

A four-step process is designed for the fabrication of the single layer microbolometer detectors. The steps are comprised of deposition and patterning of the mirror layer, the sacrificial layer, and the thermistor layer, and the removal of the sacrificial layer. All the steps are optimized separately and it is required to revise the thickness of the ZnO layer and the cavity thickness at the results of the process optimizations as 25 nm and 2.2 µm, respectively. The detectors are fabricated after the revision of the design.

Several tests are performed after the fabrication process of the single layer pixels. The TCR of the thermistor layer is measured as -10.5 %/K at 20 °C and the 1/f noise corner frequency is obtained as 302.5 Hz at 5 µA bias current. The average infrared absorption at 8-12 µm wavelength range is measured between 30 % and 39 %. The results of this study show that it is possible to implement a single layer structure for the microbolometers by using ZnO material as the active, the absorber and the structural layers to simplify the fabrication process. By improving the process steps to use a thicker ZnO layer, the performance of the single layer microbolometer detector pixels will be increased and become suitable for low-cost commercial applications.

Keywords: Uncooled infrared imaging, single layer microbolometers, ZnO microbolometers, low-cost thermal detectors.

ÖZET

TEK KATLI BİR SOĞUTMASIZ KIZILÖTESİ DEDEKTÖR PİKSELİNİN TASARIM VE KARAKTERİZASYONU

Çiğdem YILDIZAK
Elektrik - Elektronik Mühendisliği Anabilim Dalı
Danışman: Doç. Dr. M. Yusuf TANRIKULU
Haziran 2019, 76 sayfa

Bu tezde tek katmanlı bir soğutmasız mikrobolometre dedektörünün üretimi ve karakterizasyonu anlatılmaktadır. Tek katman yapısı aynı malzemeyi ısıl direnç, yapısal malzeme ve emilim malzemesi olarak kullanmak amacıyla geliştirilmiş ve bu şekilde üretim karmaşıklığını azaltarak daha düşük maliyetli bir çözüm ortaya koymak amaçlanmıştır.

Tasarım tek katman malzemesinin atomik katman kaplama yöntemi ile kaplanmış Çinko Oksit (ZnO) olarak belirlenmesiyle başlamıştır. Tek katmanlı mikrobolometre dedektör pikselinin yapısal tasarımı, tasarım parametrelerinin optik, termal ve mekanik simülasyonları yapılarak optimize edilmesiyle tamamlanmıştır. 25, 35 ve 50 µm boyutlarındaki pikseller tasarlanmış; tasarlanan piksellerin ZnO katman kalınlığı ve katmanın tabandan yüksekliği değerleri, 8-12 µm dalga boyu aralığındaki emilim değeri %85'den yüksek olacak şekilde optimize edilmiştir. Tasarlanan piksellerin ısıl iletkenliklerinin $0.5x10^{-6}$ ile $7.7x10^{-6}$ W/K arasında ve ısıl zaman sabitlerinin de 0.2 ile 2.8 ms arasında değiştiği simüle edilmiştir.

Tek katmanlı mikrobolometre dedektörleri için dört adımlı bir fabrikasyon süreci tasarlanmıştır. Bu adımlar ayna katmanı, feda katmanı ve ısıl direnç katmanının serilip şekillendirilmesi ile feda katmanının kaldırılmasından oluşmaktadır. Tüm adımlar ayrı

ayrı optimize edilmiş ve bunun sonucunca ZnO katmanın kalınlığının ve katmanın tabandan yüksekliğinin sırasıyla 25 nm ve 2.2 µm olarak revize edilmesi gerekmiştir. Tasarımın revize edilmesinin ardından dedektörlerin üretimi yapılmıştır.

Tek katmanlı piksellerin fabrikasyon süreci tamamlandıktan sonra bazı testler yapılmıştır. Testlerin sonucunda TCR değeri 20 °C'de -10.5 %/K olarak, 1/f gürültüsünün köşe frekansı da 5 µA akım uygulanarak 302.5 Hz olarak elde edilmiştir. 8-12 µm dalgaboyundaki ortalama kızılötesi emilim %30 ile %39 arasında ölçülmüştür. Çalışmanın sonuçları, ZnO malzemesinin aktif, emilim ve yapısal katmanlar yerine kullanılmasıyla, tek katmanlı mikrobolometre yapısının fabrikasyon sürecini basitleştirmek amacıyla uygulanabilir olduğunu göstermiştir. Fabrikasyon adımlarının daha kalın bir ZnO katman elde edebilmek için geliştirilmesiyle, tek katmanlı mikrobolometre dedektör piksellerinin performansı artırılacak ve düşük maliyetli ticari uygulamalar için kullanıma uygun hale getirilmiş olacaktır.

Anahtar Kelimeler: Soğutmasız kızılötesi görüntüleme, tek katmanlı mikrobolometreler, ZnO mikrobolometreler, düşük maliyetli termal dedektörler.

To my family

ACKNOWLEDGEMENTS

I would like to start with expressing my gratitude to my supervisor Assoc. Prof. Dr. M. Yusuf Tanrıkulu for his extreme support, guidance, and patience in every moment of this study. I feel lucky to have a chance to work with him.

I appreciate Prof. Dr. Tayfun Akın to give me the chance to join the fabrication process of this thesis in METU MEMS Research Center. I learned so many things during the time I spent there. I am also grateful to Orhan Akar to deal with me in the clean room and share his extensive knowledge despite his extreme workload. He inspired me with his great working discipline and wide experience.

I would like to thank Adem Saraç, Ramazan Çetin, Mustafa Yıldırım, Murat Yağcı, Akın Aydemir, and Selçuk Keskin for their supports during the fabrication process and tests. I also want to thank Ertuğ Şimşek, Baran Tekin, Emre Ersoy, Buğra Gülcüler, Meltem Okan, Batuhan Beşcan, and Semih Çavdar for their friendships. I also want to thank all other METU MEMS Research Center family members for their hospitality.

I would like to thank Yusuf Aykut Ergin and Bilal Taş who were my managers in the company that I previously worked for. They have always been more than a manager for me with their great personality, endless encouragement, advice, and friendship. I also want to thank my closest friend Serpil Kayacı for being more than a friend, being like a sister to me.

I want to express my deepest appreciation to my mother Nimet Yıldızak, my father Erol Yıldızak, and my brother Göksel Yıldızak to not only supporting me about my education but also in every detail of my entire life. Finally, I want to thank our cat Hera to give me peace, love, and motivation that I need for writing this thesis.

This thesis was financially supported by TÜBİTAK with project number of 114E645.

TABLE OF CONTENTS

LIST OF TABLES

LIST OF FIGURES

1. INTRODUCTION

Solar energy is in the form of wide spectrum electromagnetic wave. Some wavelengths are absorbed and some are reflected when the light falls on to an object. Reflection or absorption at a wavelength depends on the material property of the object. When reflected wavelengths reach the human eye, the photoreceptor cells, which act as biological sensors that can convert the visible light into signals, initialize the seeing activity. These cells need to be triggered by light to generate a signal. This is the reason that we need light to initialize the seeing activity. Even if we cannot see in the dark by our eyes, there is an alternative way to see by using an imaging equipment.

Every object which is at a temperature above absolute zero radiates depending on the material properties of the object (Lloyd, 1975). This radiation can be sensed by infrared imaging devices and this allows us to see in the total darkness. Since infrared imaging is based on sensing the thermal radiation emitted by the objects, it is not only used to see in the dark but also it has other usage areas. Beside of main usage areas such as military, astronomy, medical systems, firefighting, marine, surveillance, and automotive; applications of infrared imaging are spreading from day to day depending on improvements of infrared detectors which provide lower cost, small size, and higher performance (Yole Développement, 2017). This thesis study consists of developing a single layer uncooled microbolometer as a simplified infrared detector structure to reduce manufacturing steps and dependently to reduce the cost.

In the following sections of this chapter, detailed information about infrared systems is given. Section 1.1 introduces the theory of infrared systems. Section 1.2 gives a general overview of the infrared detectors family. In section 1.3, branches of uncooled infrared detectors are described. Section 1.4 focuses on the microbolometers and gives the performance parameters for microbolometers. At the end of this chapter, section 1.5 presents the research objectives and thesis organization.

1.1. Infrared Radiation

The electromagnetic spectrum is a combination of all types of electromagnetic waves. It is categorized by the wavelengths as radio wave, microwave, infrared, visible, ultraviolet, x-ray, and gamma-ray wavebands. Infrared radiation is an electromagnetic wave which has a wavelength range lying above the visible spectrum, around 700 nm - 1 mm. This range is divided into sub-wavebands as near-infrared (NIR), short-wave infrared (SWIR), mid-wave infrared (MWIR), long-wave infrared (LWIR), and far infrared (FIR).

Although there are no strict borders between the wavebands of the electromagnetic spectrum, it is generally accepted as NIR from 0.74 to 1.4 µm, SWIR from 1.4 to 3 µm, MWIR from 3 to 8 µm, LWIR from 8 to 15 µm, and FIR from 15 to 1000 µm ("https://en.wikipedia.org/wiki/Infrared," 2019). Figure 1.1 illustrates the electromagnetic spectrum and sub-regions of the infrared waveband.

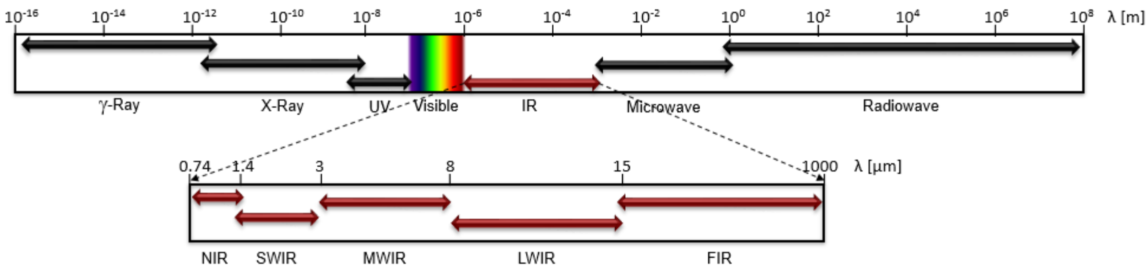

Figure 1.1. Electromagnetic spectrum and sub-regions of the infrared waveband.

Electromagnetic radiation is absorbed, scattered, and refracted by the components in the atmosphere such as gases and particles. As an example, water vapor is very strong absorber around 5.5-7.5 µm range which is in the infrared spectrum, and carbon dioxide absorbs in mid and far infrared regions. These result in the attenuation of the radiation (Holst, 2000). In the infrared spectrum, there are regions that there is almost no atmospheric transmission. Regions with low absorption, called atmospheric transmission window, occurs at 3-5 µm and 8-12 µm wavelength ranges. Therefore, infrared detectors are generally designed to operate in these wavelength ranges.

Beside of considering the atmospheric transmission bands while designing an infrared imaging system, the temperature range of the target should also be considered since the emitted radiation depends on the temperature of the object. The emissivity of an object is theoretically maximum if it is a blackbody. Therefore, by investigating the spectral radiant exitance of a blackbody, the wavelength range that allows maximum emissivity can be determined (Rogalski, 2011). The spectral radiant exitance of a blackbody is described by Planck's law as follows:

$$M(\lambda, T) = \frac{2\pi hc^2}{\lambda^5(e^{hc/\lambda kT} - 1)} \tag{1.1}$$

where M is the spectral radiant exitance, h is the Planck's constant, c is the speed of the light, λ is the wavelength, k is the Boltzmann's constant, and T is the temperature of the blackbody.

The wavelength where the spectral radiant exitance becomes maximum, shifts depending on the temperature. The wavelength that the radiant exitance reaches the peak value at a temperature is indicated by Wien's displacement law as:

$$\lambda_{max} = \frac{2898}{T} \tag{1.2}$$

where λ_{max} is the wavelength of the maximum radiant exitance in µm and T is the temperature of the object in K. Figure 1.2 shows the spectral radiant exitance at different temperatures and Wien's displacement curve. The points which the Wien's curve intersects the exitance curves are the peak exitance values at the related temperatures. As seen, at the room temperature, the wavelength that makes the exitance maximum is around 10 µm. This is the main reason of designing the detectors to operate at 8-12 µm to sense objects at the room temperature.

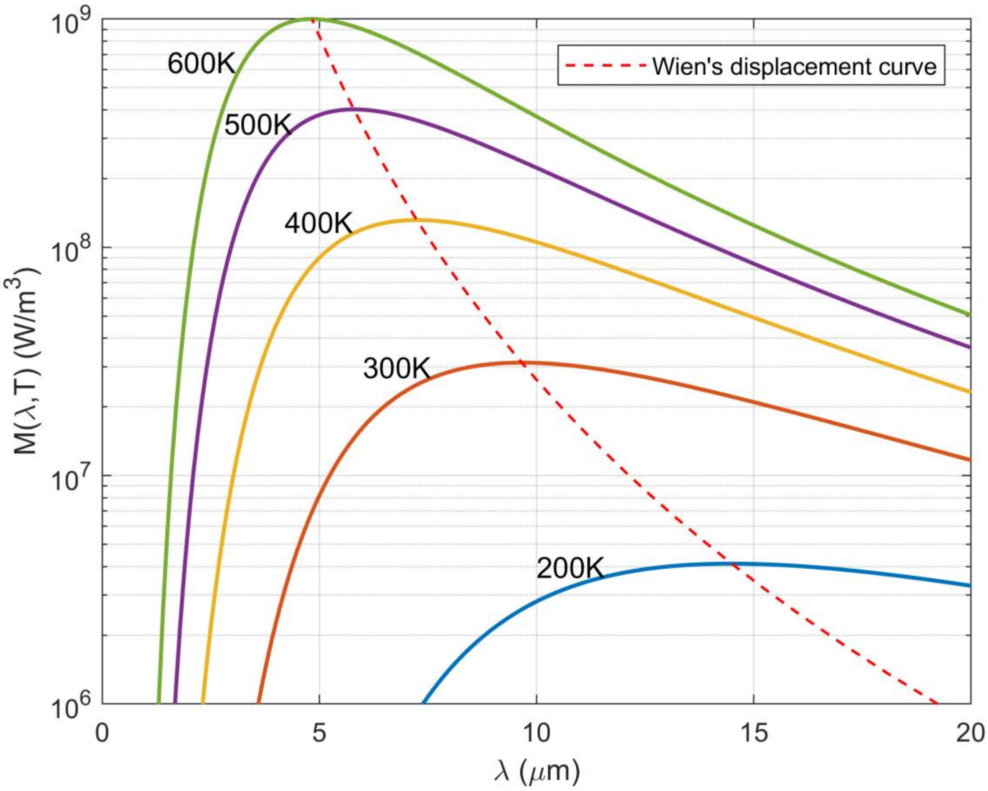

Figure 1.2. Spectral radiant exitance for different temperatures and the Wien's displacement curve.

1.2. Overview of Infrared Detectors

Infrared detection systems are categorized into two main bases as photon detectors and thermal detectors. Photon detectors work in principle of absorbing photons and producing current or voltage depending on the amount of the absorbed photons (David, 2006). As mentioned in the previous section, to sense the objects that are in the room temperature, the detector should operate at 8-12 µm waveband which is in the long-wave infrared region. In this region, the photons have low energy. To detect these low energy photons, the energy required for the electron transition to be free-charge carrier should be lower than the photon energy. Since the transition energy is comparable with the thermal energy at the room temperature, long-wave infrared detectors become very noisy (Piotrowski & Rogalski, 2007). At this point, cooling becomes a solution to overcome this issue. Because of the cooling requirement, this type of detectors are also known as cooled detectors.

In the thermal detectors, sensing is performed by measuring the effect of the temperature change, caused by the absorbed photons, upon the detector material (Kruse & Skatrud, 1997). In the detection process, there is no relation between incoming photon energy and the transition energy to generate free electrons in the material. Hence, there is no cooling requirement in these type of detectors, and they are also named as uncooled detectors (P.W.Kruse, 1999).

Photon detectors can be grouped depending on the interaction mechanism of photons or development mechanism of the electric and magnetic field. Depending on the interaction mechanism of photons, they can be categorized as intrinsic detectors, extrinsic detectors, photoemissive detectors, and quantum well detectors; and by looking up to the development mechanism of the electric or magnetic field, they can be grouped as photoconductive, photovoltaic, and photoemissive detectors (Henini & Razeghi, 2002; Kinch, 2007; Rogalski, 2003). Thermal detectors are mainly categorized as thermopiles, pyroelectric detectors, and microbolometers.

Both photon and thermal detectors have several advantages and disadvantages. Photon detectors are known by exhibiting very fast response and high signal to noise ratio. In order to provide these advantages, they need cryogenic coolers, and the cooling requirement increases the cost, power consumption, and weight. Since the thermal detectors do not need cooling, they have low cost, low power consumption, and low weight. Opposed to these advantages, they provide low performance and slow response ("http://www.flirmedia.com/MMC/CVS/Tech_Notes/TN_0005_EN.pdf," 2019).

Considering the characteristic properties, photon detectors are generally used in the applications which the performance is more important than the cost while the thermal detectors are generally preferred for low-cost applications.

1.3. Thermal Infrared Detectors

The thermal detectors work in principle of measuring the heating effect of the infrared radiation on the detector material. Figure 1.3 represents the general structure of a thermal infrared detector. The structure mainly consists a substrate that acts as a heat sink, a sensor area which absorbs the infrared radiation and reacts by changing its temperature, and a readout circuit to process the temperature change of the detector.

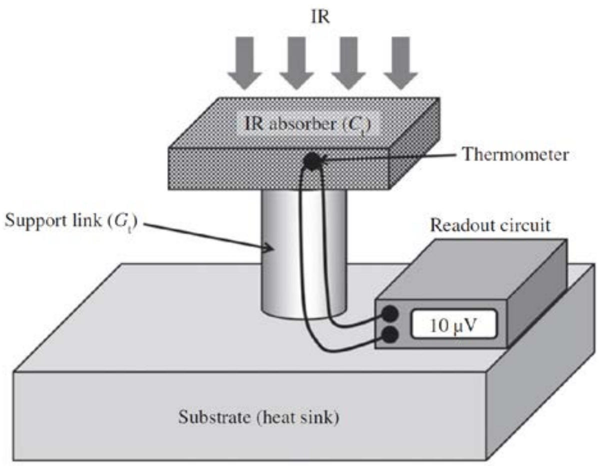

Figure 1.3. The general structure of a thermal infrared detector (Kimata, 2018).

Since detection of the infrared radiation is performed by an indirect way, heating of the sensing area and reading of the temperature difference takes more time, therefore the response time of the detector increases and the performance decreases. However, the features such as low cost, low power dissipation, and compactness allow the uncooled detectors to be used in many areas and attracts researchers to investigate the ways to increase the performance.

Considering their working principles, the thermal infrared detectors can be investigated under three main categories; thermoelectric detectors (thermopiles), pyroelectric detectors, and microbolometers. The types of thermal detectors are detailed in the following sections.

1.3.1. Thermopile detectors

A thermopile detector is a combination of several thermocouples that convert temperature change caused by infrared absorption to a voltage output by Seebeck effect. Figure 1.4 illustrates a thermocouple structure. In this type of detectors, two separate electrical conductors which have different Seebeck coefficients are used to induce a potential difference. The junction side of the conductors is heated by the incoming infrared radiation, and from the open-ended side, the voltage difference is measured by a readout circuit (Lei et al., 2016).

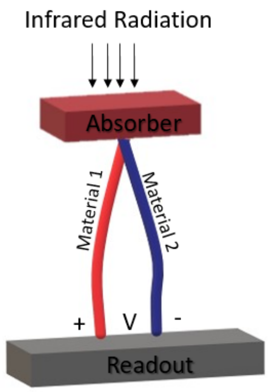

Figure 1.4. Typical structure of a thermocouple.

The voltage difference caused by the Seebeck effect is found as,

$$V_{out} = (\alpha_1 - \alpha_2)\Delta T \tag{1.3}$$

where V_{out} is the output voltage at the open-end of the thermocouple, α_1 and α_2 are the Seebeck coefficients of the material 1 and material 2, respectively, and ΔT is the temperature difference between the hot junction and the cold open-end of the materials (Xu, Wang, Xiong, & Li, 2017). Since the voltage difference induced by only one thermocouple is not enough to detect the infrared radiation, the thermocouples are connected in series to be in the form of a thermopile.

By this way, the voltage delivered to the output is increased, and detecting the infrared radiation can be possible (Escriba, Campo, Estève, & Fourniols, 2005). Thus, the voltage generated by a thermopile can be written as,

$$V_{tp} = NV_{out} = N(\alpha_1 - \alpha_2)R_{th}\eta P_0 \quad (1.4)$$

where V_{tp} is the output voltage of the thermopile, N is the number of the thermocouples connected in series, V_{out} is the output voltage of one thermocouple, R_{th} is the thermopile's thermal resistance, η is the absorption coefficient, and P_0 is the radiative power collected by the absorbing area. The responsivity of the detector is defined by the ratio of the generated voltage across the thermopile over the incoming radiative power, denoted by $\Re_v$:

$$\Re_v = \frac{V_{tp}}{P_0} \quad (1.5)$$

To increase the thermopile output voltage and dependently the detector responsivity, the materials should be chosen so that the Seebeck coefficient difference to become maximum. Since increasing the thermocouple number also increases the thermal conduction between hot and cold junctions, and the thermopile resistance, it will also cause an increase in the noise which is an undesired result (Brand & Fedder, 2005). Therefore, the thermocouple number should be optimized and should not be increased haphazardly.

Although the thermopiles have low sensitivity and large size when compared with bolometers and pyroelectric detectors, the advantages such as operation without electrical bias and temperature stabilization make them used in various applications (Graf, Arndt, Sauer, & Gerlach, 2007; Kruse, 2001; M. Yusuf Tanrikulu, 2007).

1.3.2. Pyroelectric detectors

Pyroelectric detectors are in the form of a capacitor that composes of two parallel metal electrodes with a pyroelectric material between them. Figure 1.5 illustrates the structure of a pyroelectric detector. The sensing of the infrared radiation is performed by the pyroelectric property of the material. Initially, the pyroelectric material is unpolarized. When the infrared radiation falls on to the detector area, the pyroelectric material is polarized as a consequence of the temperature increase. The polarization of charges induces a current if the electrodes are connected to an external circuit (Tiffany, 1975). The generated current is proportional to the rate of change of the temperature and formulated by,

$$I = p(T)A\frac{dT}{dt} \tag{1.6}$$

where I is current induced by charge polarization, $p(T)$ is the pyroelectric coefficient at temperature T, A is the detector area, and dT/dt is the rate of temperature change.

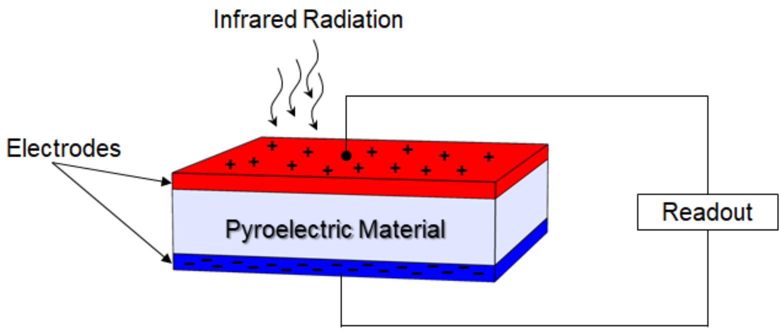

Figure 1.5. Structure of a pyroelectric detector.

Since the detection process requires a change in the temperature, when the radiation falls on to the detector steadily, dT/dt parameter goes to zero. Hence, the current generation is interrupted. To overcome this issue, pyroelectric detectors require an optical chopper to modulate the continuous flux (Gaussorgues, 1994). This is the main limitation for the pyroelectric detectors. Even so, in some applications such as detecting the motion, usage of the pyroelectric detectors can be ideal because the detector does not respond to the stationary sources; it only responses to the movement (Boreman, 2016).

1.3.3. Microbolometers

Microbolometers realize the detection process by measuring the change of an electrical property affected by the infrared radiation like the other thermal detectors. Depending on the sensing material type, the microbolometers are divided into two groups as resistive type and diode type microbolometers. In the diode type microbolometers, infrared radiation is sensed by reading the forward voltage change caused by heating. In the resistive type microbolometers, the detector material changes its resistance due to the radiation heating. Diode type microbolometers stay in the back of the resistive type microbolometers since they have relatively low sensitivity, low fill factor and high time constant (Senveli, 2010). Since a resistive type microbolometer detector is the subject of this thesis, they are detailed in the rest of the chapter.

Microbolometers are constructed on a bridge structure consisting of a resistive material isolated from the substrate by the support arms. Figure 1.6 represents the typical structure of a microbolometer. The resistive material changes its resistance due to the heating effect of the absorbed radiation as the infrared radiation falls on to the detector. The change of the resistance is determined by a readout integrated circuit that is located below the suspended active detector area.

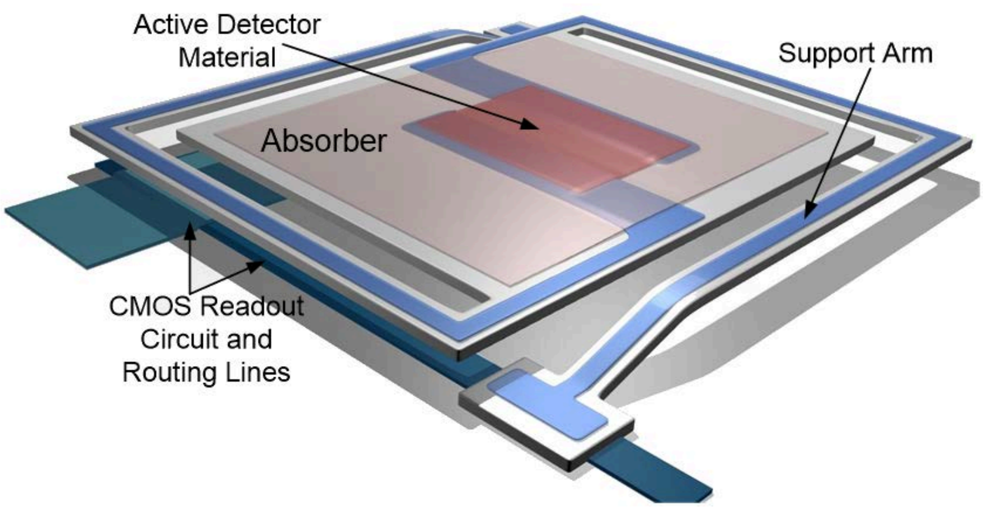

Figure 1.6. Typical structure of a microbolometer detector (M. Yusuf Tanrikulu, 2007).

Vanadium oxide (VO_x) and amorphous silicon (a-Si) is commonly used active materials in the microbolometers (Tissot et al., 2010; Voshell, Dhar, & Rana, 2017). Beside them, there are other various materials that are used as active material such as yttrium barium copper oxide (YBaCuO) (Jahanzeb, Travers, Çelik-Butler, Butler, & Tan, 1997), silicon germanium (SiGe) (Dong, Yue, & Liu, 2003), silicon carbide (SiC_x) (Ichihara, Watabe, Honda, & Aizawa, 1997), platinum (Pt) (Shie, Chen, Ou-yang, & C. S. Bruce, 1996), titanium (Ti) (R. S. Saxena, Bhan, Jalwania, & Khurana, 2008), and graphene (GR) (Ryzhii et al., 2013). Table 1.1 shows the TCR values of these materials taken from the various applications reported in the literature.

Table 1.1. Examples of the temperature coefficient of resistance values from various materials reported in the literature.

Material	**|TCR| (%/K)**	**Reference**
VO_x	2 - 5.6	(Wang, Lai, Li, Hu, & Chen, 2013)
a-Si	2 - 4.9	(Ajmera, Syllaios, Tyber, Taylor, & Hollingsworth, 2010; Syllaios et al., 2000)
SiGe	2 - 5	(Atar, Yesilyurt, Onbasli, Hanoglu, & Okyay, 2011)
YBaCuO	3.2 - 3.4	(Travers, Jahanzeb, Butler, & Çelik-Butler, 1997; Wada et al., 2001)
SiC_x	0.7 - 2.3	(Niklaus, Vieider, & Jakobsen, 2007; Tsutsumi, Yamashita, & Ohji, 2002)
Pt	0.14 - 0.39	(Tsutsumi et al., 2002; Yoneoka, S., Liger, M., Yama, G., Schuster, R., Purkl, F., Provine, J., Prinz, F. B., Howe, R. T., and Kenny, 2011)
Ti	0.28	(Raghvendra Sahai Saxena et al., 2011)
GR	3	(Liang, 2014)

In the most of the uncooled detector applications, silicon nitride (Si_3N_4) (Erturk, Battal, Kucuk, Okyay, & Akin, 2013), gold black (Wang, 2012), nichrome (NiCr) (Ehab S. Awad, Al-Khalli, Abdel-Rahman, Alduraibi, & Debbar, 2015), titanium (Ti) (Cheng, Paradis, Bui, & Almasri, 2009), vanadium pentaoxide (V_2O_5) (E. S. Awad, Al-Khalli, Abdel-Rahman, Debbar, & Alduraibi, 2015) are used absorber materials; gold (Au) (Kebapci, Dervisoglu, Battal, Okyay, & Akin, 2014), aluminum (Al) (Perera, 2012), titanium (Ti) (Perera, 2012) are used as reflector materials, and silicon nitride is used as structural layer material.

The ongoing studies investigate the ways of decreasing the cost together with increasing the performance. Pixel size reduction, finding new materials or developing alternative structural designs are being studied to enhance the uncooled infrared systems.

1.4. Performance Parameters of the Microbolometers

There are some parameters that specify the performance of a microbolometer such as temperature coefficient of resistance, thermal conductance, thermal time constant, responsivity, noise equivalent temperature difference, and noise equivalent power. In the next subsections, these parameters are detailed.

1.4.1. Temperature Coefficient of Resistance

Temperature coefficient of resistance (TCR) is the main figure of merit for the thermistor material of the detector. It is a parameter that shows how the resistance of the thermistor material of a microbolometer changes depending on the temperature. TCR is represented by;

$$\alpha = \frac{1}{R}\frac{dR}{dT} \qquad (1.7)$$

where α is TCR with a unit of %/K, R is the resistance of the detector, and $\frac{dR}{dT}$ is the rate of change of the resistance due to the temperature. Depending on the increasing or decreasing tendency of the resistance with temperature, the TCR can be positive or negative. As the absolute value of the TCR becomes higher, the sensitivity of the detector also becomes higher.

1.4.2. Thermal Conductance

Thermal conductance is a parameter to show how well the suspended area of the detector is thermally isolated from the substrate. Since it represents heat loss at the thermal sensing area; lower thermal conductance means better isolation and hence better performance. There are three main heat loss sources for the microbolometers: heat loss by the support arms that provide a bridge between the substrate and the sensing area, heat loss due to the emitted radiation by the detector itself, and the loss between the detector and the gaseous environment that surrounds the detector (Eriksson, Andersson, & Stemme, 1997). Hence, the total thermal conductance of a microbolometer can be represented by;

$$G_{th} = G_{arms} + G_{rad} + G_{gas} \tag{1.8}$$

where G_{th} is the total thermal conductance of the detector, and G_{arms}, G_{rad}, and G_{gas} are the thermal conductance components of the arms, radiation, and the gaseous environment, respectively. If a microbolometer has n arms and each arm consists layers of m different materials, the thermal conductance through the arms of the detector is formulated as,

$$G_{arms} = n \sum_{i}^{m} \frac{\kappa_i A_i}{l} \tag{1.9}$$

where n is the number of the arms of the detector, κ_i is the thermal conductivity of the i^{th} material consisted by arms, A_i is the cross-sectional area of the i^{th} arm material, and l is the length of the arm (Niklaus, Decharat, Jansson, & Stemme, 2008). The radiative component of the thermal conductance is given by,

$$G_{rad} = 4 A_D \eta \sigma T^3 \tag{1.10}$$

where A_D is the absorbing area of the detector, η is the emissivity of the detector, σ is the Stefan-Boltzmann constant, and T is the temperature of the detector.

Finally, the gaseous environmental component of the thermal component can be represented as,

$$G_{gas} = \frac{\kappa_{gas} A_D}{d} \qquad (1.11)$$

where κ_{gas} is the thermal conductivity of the environmental gas, A_D is the active detector area, and d is the cavity thickness between the active area and the substrate.

Thermal conductivity of the environmental gas is very close to zero due to the vacuum conditions of the detector. Hence, the thermal conductance component of the gaseous environment approaches to zero and becomes negligible in comparison to the thermal conductance of the arms. The radiative component is also negligibly small behind the thermal conductance of the arms. Thus, the total thermal conductance of the detector usually calculated only by the thermal conductance of arms (Bhan, Saxena, Jalwania, & Lomash, 2009). Using materials that have low thermal conductivity for arms, keeping the arm length long, and reducing the pixel active area also reduce the thermal conductance. But since these parameters affect the other performance parameters, the thermal conductance is optimized considering the related parameters.

1.4.3. Thermal Time Constant

Thermal time constant is another important performance parameter for microbolometers. It indicates how fast the detector gives a response to the infrared radiation. It is expressed by,

$$\tau = \frac{C_{th}}{G_{th}} \qquad (1.12)$$

where τ is the thermal time constant, C_{th} is the thermal capacitance of the detector in J/K, and G_{th} is the thermal conductance in W/K.

The thermal capacitance of a detector that contains n layer of different materials can be determined by,

$$C_{th} = \sum_{i}^{n} V_i \rho_i c_i \tag{1.13}$$

where V_i is the volume, ρ_i is the density, and c_i is the specific heat of the ith layer of the detector. As seen from the equations, the thermal time constant directly depends on the pixel geometry. Moreover, there is a tradeoff between the thermal conductance and the time constant since as the thermal conductance decreases, the time constant increases.

The thermal time constant should also be optimized considering the imaging frame rate of the system. It should be lower than the reciprocal of the frame rate. In the widespread applications of the microbolometers, the detectors are usually designed to have a thermal time constant value of lower than one-third or half of the $\frac{1}{frame\ rate}$ (Bhan et al., 2009; Li, Skidmore, Howard, Clarke, & Han, 2009; Yon, Mottin, & Tissot, 2008).

1.4.4. Responsivity

Responsivity expresses the electrical response of the detector and defined as the ratio of the output power of the detector to incoming infrared power. The unit of the responsivity can be V/W or A/W with regard to voltage or current dependency of the readout method. The voltage responsivity ($\Re_V$) and the current responsivity ($\Re_I$) of a microbolometer detector is formulated as below, respectively,

$$\Re_V = \frac{\Delta V}{P_{in}} = \frac{\eta I_d \alpha R_d}{G_{th}\sqrt{1 + (\omega\tau)^2}} \tag{1.14}$$

$$\Re_I = \frac{\Delta I}{P_{in}} = \frac{V_d \alpha \eta}{R_d G_{th}\sqrt{1 + (\omega\tau)^2}} \tag{1.15}$$

where P_{in} is incoming infrared power, ΔV and ΔI are the voltage and the current change at the output of the detector induced by the absorbed radiation, V_d and I_d are the bias voltage and current of the detector, respectively. η is the absorptance, α is the TCR, R_d

is the resistance, G_{th} is the thermal conductance, τ is the thermal time constant of the detector, and ω is the modulation frequency of the infrared power.

To design a high-performance detector, the responsivity value should be optimized to be high. As seen by the equations, material choice and structural design have critical importance since the TCR, the absorptance, and the thermal conductance directly affect the responsivity.

1.4.5. Noise Equivalent Temperature Difference

Noise equivalent temperature difference (NETD) expresses the minimum detectable temperature difference that distinguishes the target from its background. This parameter is not only a measure for the detector, but it also includes the optical information of the overall system. It is determined by,

$$NETD = \frac{4F^2 V_n}{\tau_o A_D \Re_V (\Delta P/\Delta T)_{\lambda_1 - \lambda_2}} \tag{1.16}$$

where F is a function of focal length and the diameter of the optics, V_n is the total rms noise voltage, τ_o is the transmission of the optics, A_D is the active detector area, $\Re_V$ is the voltage responsivity, $(\Delta P/\Delta T)_{\lambda_1 - \lambda_2}$ is the change of the power per unit area radiated by a blackbody at temperature T, measured within the spectral band of $\lambda_1 - \lambda_2$ (M. Yusuf Tanrikulu, 2007). It is important to minimize the NETD to design a high-performance infrared system.

1.4.6. Noise Equivalent Power

Noise equivalent power (NEP) is another parameter that helps to determine the detector performance. It is defined as input power generated by the absorbed radiation that makes the signal to noise ratio (SNR) equals to one (Wolfe, 1996). The NEP is determined with,

$$NEP = \frac{V_n}{\Re_V} \tag{1.17}$$

where V_n is the total rms noise and $\Re_V$ is the voltage responsivity.

1.5. Research Objectives and Thesis Organizations

In this study, it is aimed to construct a cost-effective solution for low-cost applications by simplifying the pixel structure and usage of an alternative material for the detector. Through this aim, design and characterization of a single layer microbolometer that consists of only ZnO material instead of using various materials for the active material, the absorbing layer, and the structural layer are performed.

The outline of this study can be investigated under three main parts. In the first part, the design of the single layer microbolometer is performed. Determination of the active material that is used as the single layer, the geometrical design of the detector, and the optimization of the structural parameters by conducting the optical, thermal and mechanical simulations are realized in this first part. Chapter 2 explains the design steps of a single layer microbolometer that make detectors become ready to be fabricated.

In the next part, fabrication and optimization of the designed detectors are realized. The design of the fabrication process steps is presented and by considering the issues that are faced in these fabrication steps, the detector designs are optimized to become suitable for production. Chapter 3 presents the details of this part.

After the fabrication process is completed, the tests of the produced pixels are executed in the third part. Chapter 4 gives the test results of the detectors.

Finally, Chapter 5 summarizes all of the parts and concludes the study by giving the future works to enhance the results.

2. DESIGN OF A SINGLE LAYER MICROBOLOMETER

Designing a microbolometer consisting of different layers is a complex issue as told in the previous chapter. Using the same material for the thermistor layer, the absorber layer and the structural layer reduces the design complexity of the microbolometer. However, there are still many issues to be considered during the design process. Since the thermistor material will also be used as the absorber and the structural layers, the most important thing is deciding on the material that will be used as a single layer. Second important consideration is the mechanical structure of the detector. The bridge should be designed to be strong enough to carry the structure, the active area should be well isolated from the substrate, and the single layer should be fabricated in an appropriate way to have unbuckled detectors. Another design parameter is the cavity thickness between the substrate and the suspended area. This thickness should be optimized to have maximum absorption in the targeted wavelength range. The other issue is finding a material that has a good ohmic contact with the chosen thermistor material to decrease the connection resistance.

This chapter presents the design stages of a single layer microbolometer detector pixel. Section 2.1 explains how to determine the material that is used as a single layer. Section 2.2 gives information about the structural design parameters. In section 2.3, the optimization of the design parameters is investigated by performing the thermal, mechanical, and optical simulations. Finally, the conclusion section summarizes the chapter.

2.1. Determination of the Single Layer Material

The material that is used as the single layer should have the properties of active material, an absorber layer, and a structural layer. Thereby, the material should have high TCR and high absorption coefficient to obtain high responsivity, low internal stress to have unbuckled structures, and low electrical noise (M. Yusuf Tanrikulu et al., 2018).

The first and most important decision parameter is TCR. In most of the microbolometer applications, the TCR values of the resistive material change in the range of 2-4 %/K. Studies show that the TCR value of active material can be improved in many ways, such as doping or changing the fabrication parameters of the material. By these investigations, the TCR values of the materials used in microbolometers are increased up to ~6 %/K as indicated in the previous chapter. As one of the most commonly used materials, VO_x needs annealing at a high temperature to have an improved TCR causes a problem with CMOS integration. In the forms of VO_x that are grown at CMOS compatible temperatures, the TCR becomes very low (Ambrosio et al., 2010). In addition to this, since the usage of the VO_x is restricted by the patents, it becomes hard to work with it (Wood, 1995). The other popular materials such as a-Si, poly-SiGe, SiC_x has a similar issue with the VO_x since the low-temperature grown forms have worse electrical properties than the high-temperature grown forms (Dong et al., 2003; Ichihara et al., 1997; Niklaus et al., 2007). Another active material category is metals such as platinum and titanium. These are CMOS compatible but the TCR values of these materials are quite low when compared with the other microbolometer materials.

The single layer microbolometer structure is firstly tried by using an atomic layer deposited platinum film of 7 nm since it presents low 1/f noise and sufficient absorption (Yoneoka, S., Liger, M., Yama, G., Schuster, R., Purkl, F., Provine, J., Prinz, F. B., Howe, R. T., and Kenny, 2011). However, this material has a TCR value of 0.14 %/K and it is not a suitable resistive material to obtain high-performance detectors.

Recently, the electrical and optical properties of the zinc oxide (ZnO) material are investigated to see if it is suitable to use as microbolometer material (Battal, Bolat, Tanrikulu, Okyay, & Akin, 2014). According to the reported study, the ZnO films are grown by atomic layer deposition method at 120, 200 and 250°C. It is seen that the

ZnO film coated at 120°C has a TCR value of -10.4 %/K at room temperature while the ZnO films that are coated at 200 and 250°C have TCR values approximately zero. It is also reported that the ZnO coated at 120°C has high absorption characteristics and low noise (Kesim, Battal, Tanrıkulu, & Okyay, 2014). Considering its great TCR value and promising absorption trend together with having low noise and low stress, it is thought that this material can be a great candidate to be used as a single layer material.

2.2. Structural Design of the Single Layer Microbolometer

In order to have a strong bridge structure, the arms of the detector should be designed to be strong enough to carry the suspended area. To achieve this, increasing the arm width and decreasing the arm length can be the first things that come to mind. But at this point, another issue arises. Since the suspended area should also be well isolated from the substrate, and the isolation is performed by the arms, the arms should not be shortened too much. The arm length and width should be optimized to achieve both good isolation and strong mechanical structure.

Since the ZnO material is used in this study as single layer material for the first time, various detectors that have different geometry are designed to overcome the possible troubles, especially during the fabrication process. The designed detectors can be categorized under the two groups as long-armed (Type 1) and short-armed (Type 2) detectors. The arm width, the arm length, the gap width between the arm and the pixel body (cavity thickness), and the pixel pitch are taken as varying parameters. The best geometries are investigated by changing these parameters. Figure 2.1 shows samples from the layout views of the long-armed and short-armed pixels and their design parameters. The detector pitch values are selected as 25, 35 and 50 µm. The detectors are designed as their arm widths change between 0.5 µm and 2.5 µm, while the gap widths change between 0.5 µm and 2 µm. Table 2.1 gives the pixels that are placed in the mask that will be used for fabrication. As can be seen from the table, there are more than 40 pixel types in order to overcome possible problems.

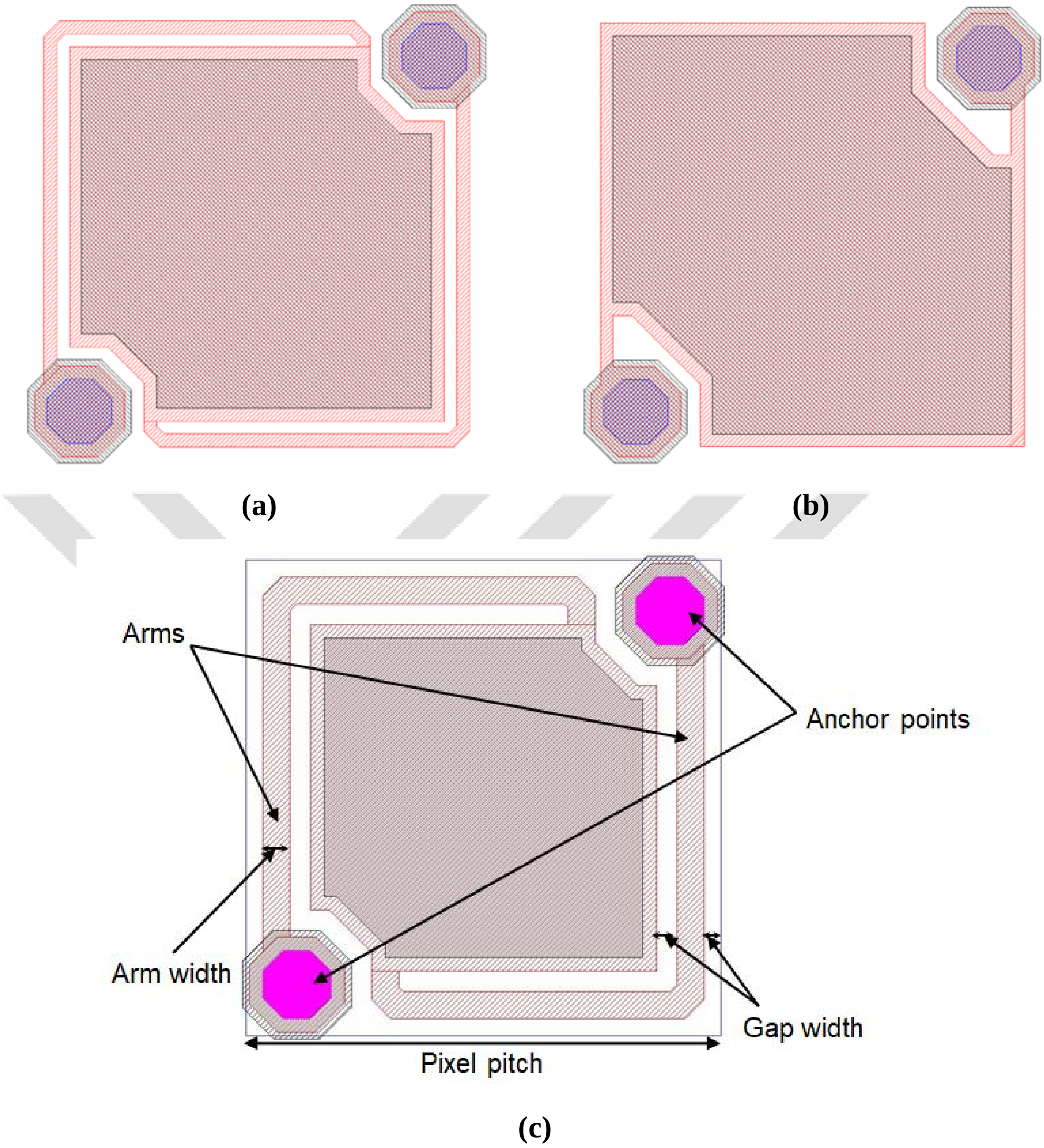

Figure 2.1. (a) Long-armed pixel (Type 1), **(b)** short-armed pixel (Type 2), and **(c)** their design parameters.

Table 2.1. The parameters of the pixels that are placed in the production mask.

Pixel Number	Pixel Type	Pitch (μm)	Arm Width (μm)	Gap Width (μm)
1	Type 1	35	0.5	0.5
2	Type 1	35	0.5	1
3	Type 1	35	0.5	1.5
4	Type 1	35	0.5	2
5	Type 1	35	1	0.5
6	Type 1	35	1	1
7	Type 1	35	1	1.5
8	Type 1	35	1	2
9	Type 1	35	1.5	0.5
10	Type 1	35	1.5	1
11	Type 1	35	1.5	1.5
12	Type 1	35	1.5	2
13	Type 1	35	2	0.5
14	Type 1	35	2	1
15	Type 1	35	2	1.5
16	Type 1	35	2	2
17	Type 1	25	0.5	0.5
18	Type 1	25	0.5	1
19	Type 1	25	1	0.5
20	Type 1	25	1	1
21	Type 1	50	1	1
22	Type 1	50	1	1.5
23	Type 1	50	1	2
24	Type 1	50	1.5	1
25	Type 1	50	1.5	1.5
26	Type 1	50	1.5	2
27	Type 1	50	2	1
28	Type 1	50	2	1.5
29	Type 1	50	2	2
30	Type 1	50	2.5	1
31	Type 1	50	2.5	1.5
32	Type 1	50	2.5	2
33	Type 2	35	1	1
34	Type 2	35	1	1.5
35	Type 2	35	1.5	1
36	Type 2	35	1.5	1.5
37	Type 2	35	2	1
38	Type 2	35	2	1.5
39	Type 2	25	1	0.5
40	Type 2	25	1	1
41	Type 2	50	2	1
42	Type 2	50	2	1.5

2.3. Simulations

After the structural designs of the detectors are completed, the parameters are optimized by the simulations. In the next subsections, the optical, the thermal, and the mechanical simulations are detailed.

2.3.1. Optical Simulations

A detector that has a high absorption also has a high responsivity and also has a better performance. The most important factors that affect the absorption amount of the detector are the refractive index (n) and extinction coefficient (k) of the absorbing materials. Besides, the thickness of the absorber material, the cavity thickness between the substrate and the single layer should also be considered to maximize the absorption amount. The absorption coefficient that is obtained from these parameters also depends on the wavelength of the incident radiation.

In this thesis study, since the single ZnO layer also operates as an absorber, the optical constants of this material are investigated, and the thickness of the single layer and its height from the substrate are optimized for the targeted wavelength range. In the literature, the optical parameters of the ZnO are investigated for using the material in a single layer microbolometer (Kesim et al., 2014). Figure 2.2 gives the graphs of dielectric permittivity, refraction index, and extinction coefficients of the ALD grown ZnO at 120°C depending on the wavelength. These parameters are used in the optical simulations of this thesis.

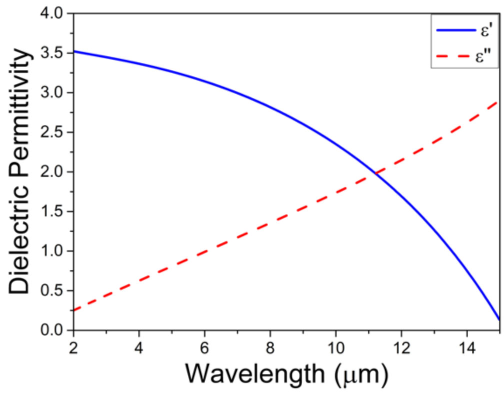

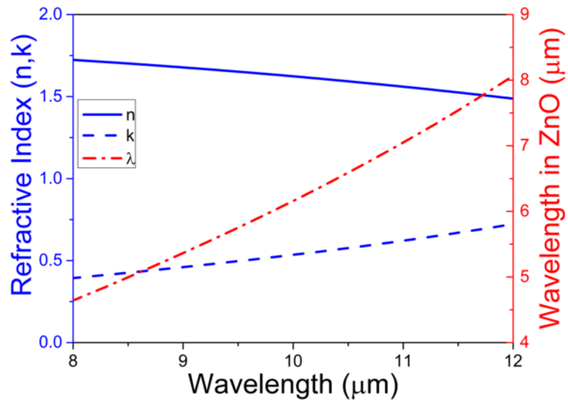

(a) **(b)**

Figure 2.2. (a) Dielectric permittivity, **(b)** refractive index and extinction coefficient of the ALD grown ZnO at 120°C depending on the wavelength (Kesim et al., 2014).

Optical simulations are performed by implementing the electromagnetic theory calculations to the multilayer detector structure with modeling the layers of the detector as a cascaded transmission line. According to theory, all layers that consisted of the detector are represented by their intrinsic impedances (M. Y. Tanrikulu, Civitci, & Akin, 2008). Figure 2.3 shows the simplified cascaded transmission line model of the single layer microbolometer.

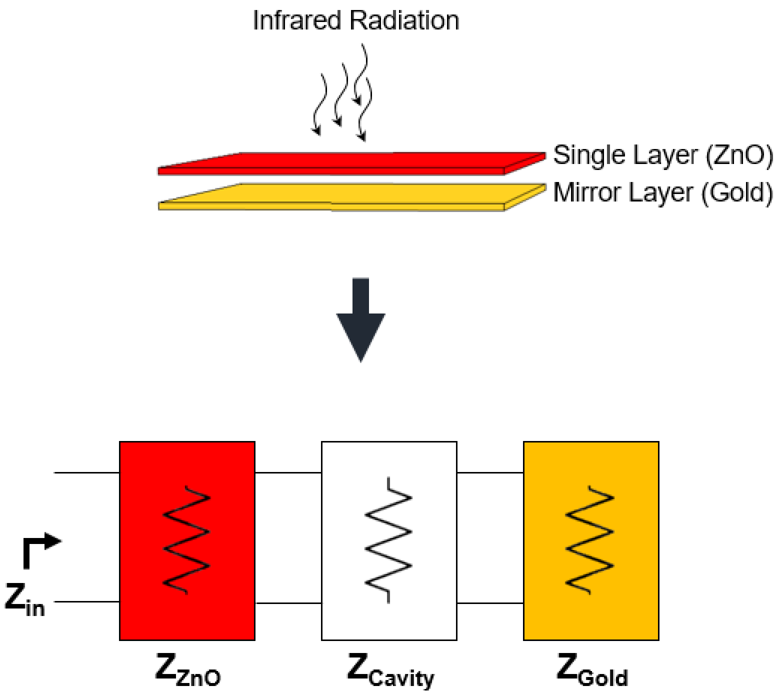

Figure 2.3. Cascaded transmission line model of the single layer microbolometer.

In the simulations, the intrinsic impedance of the ZnO layer, which can be defined as a lossy medium, is calculated by,

$$Z_{lossy\_medium} = \frac{j\omega\mu}{\gamma} \tag{2.1}$$

where ω is the radial frequency of the incident radiation, μ is the permeability of the medium, and γ is the complex propagation constant of the medium (Pozar, 2012). Since the ZnO is not a magnetic material, the permeability of the ZnO equals to the permeability of the free space. The intrinsic impedance of the cavity is taken as the characteristic impedance of free space which is 377 Ω.

After the intrinsic impedance of the layers are calculated individually, equivalent input impedance, Z_{in}, can be calculated by applying the Telegrapher's equation two times (M. Yusuf Tanrikulu, 2007). First the impedance seen from the cavity (Z_{in_cav}) is calculated as in equation 2.2, then this calculated impedance is taken as a load and the equivalent impedance seen from ZnO is calculated by applying the Telegrapher's equation second time, as in Equation 2.3, where Z_{Cavity} and Z_{Gold} are the intrinsic impedances of the cavity layer and the gold layer, γ_{Cavity} and γ_{ZnO} are the propagation constants of the cavity and the ZnO, l_{Cavity} and l_{ZnO} are the thicknesses of the cavity and the ZnO layer, respectively.

$$Z_{in\_cav} = Z_{Cavity} \frac{Z_{Gold} + Z_{Cavity} \tanh(\gamma_{Cavity} l_{Cavity})}{Z_{Cavity} + Z_{Gold} \tanh(\gamma_{Cavity} l_{Cavity})} \tag{2.2}$$

$$Z_{in} = Z_{ZnO} \frac{Z_{in\_cav} + Z_{ZnO} \tanh(\gamma_{ZnO} l_{ZnO})}{Z_{ZnO} + Z_{in\_cav} \tanh(\gamma_{ZnO} l_{ZnO})} \tag{2.3}$$

Figure 2.4 represents the infrared wave propagation through the single layer microbolometer. Since the gold layer at the bottom of the detector acts as a mirror, it is assumed that there will be no transmission through it. Therefore, the transmission coefficient (T) can be taken as zero. Then the ratio of the absorption can be expressed as,

$$A = 1 - |R|^2 \tag{2.4}$$

where R is the reflection coefficient in the complex form (Bosman, Lau, & Gilgenbach, 2003), and defined by,

$$R = \frac{Z_{in} - Z_o}{Z_{in} + Z_o} \tag{2.5}$$

where Z_{in} is the equivalent input impedance of the structure, Z_o is the characteristic impedance of free space.

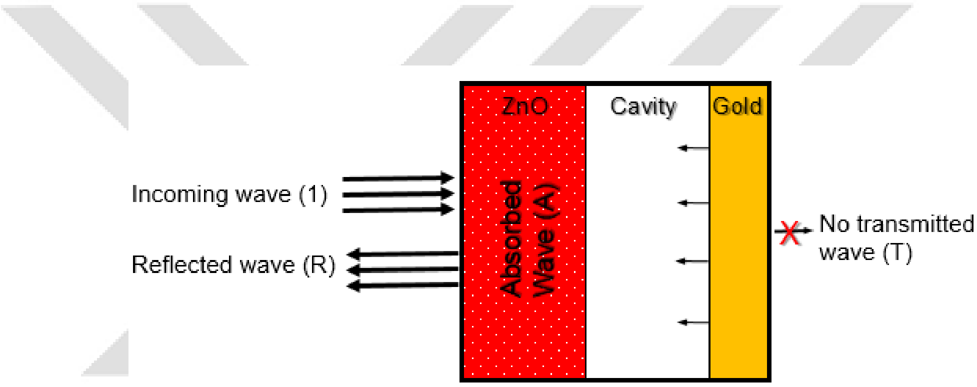

Figure 2.4. Representation of the infrared wave propagation through the single layer microbolometer.

The simulations are performed by solving the equations above using the MATLAB software. In the simulations, optimum values of the cavity thickness and the ZnO thickness are examined to make the absorption value maximum. From the results, it is seen that the thickness of the ZnO should be at least 450 nm to have an absorption amount above 85% and the corresponding cavity thickness should be 1.6 µm. Figure 2.5 gives the absorption percentage of a detector that has a 450 nm ZnO layer depending on the wavelength and the cavity thickness. For these thicknesses of ZnO and cavity, the average absorption rate at the wavelength range of 8-12 µm is extracted as 83.5% and the absorption becomes maximum at the wavelength of 10 µm as 86.8%. The detectors having such a high absorption can be used in applications requiring high performance.

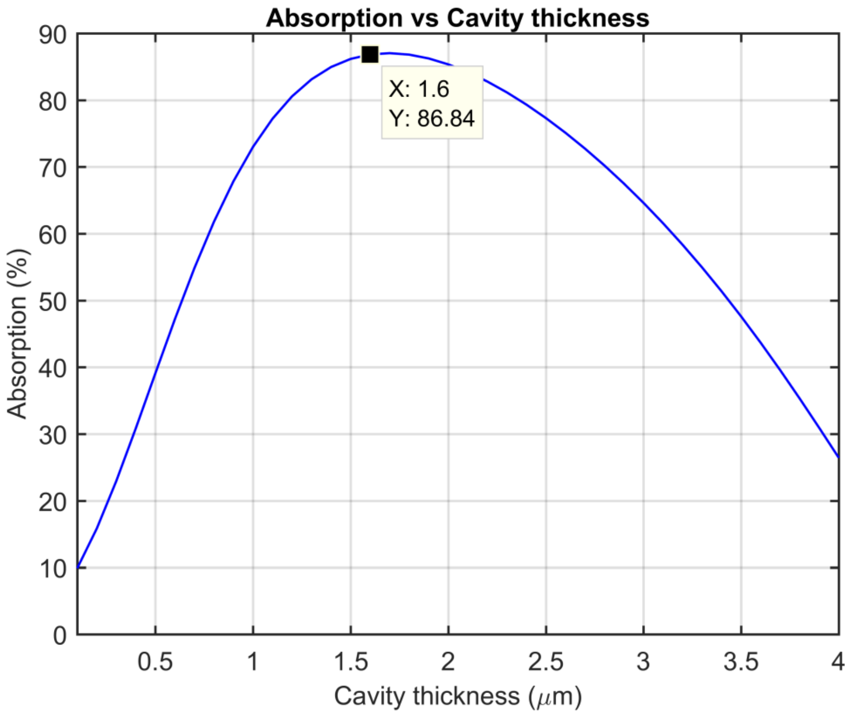

(a)

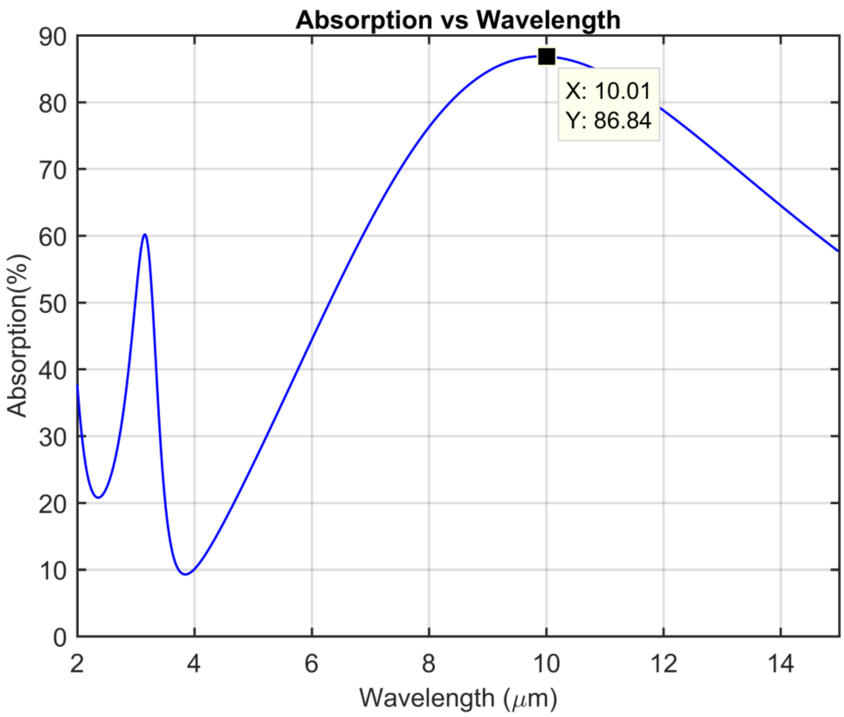

(b)

Figure 2.5. The absorption rate of a detector that has a 450 nm ZnO layer depending on **(a)** the cavity thickness and **(b)** the wavelength. The average absorption rate at the wavelength range of 8-12 µm is extracted as 83.5% and the absorption becomes maximum at the wavelength of 10 µm as 86.8%.

2.3.2. Thermal Simulations

As mentioned in the previous chapter, the thermal conductance and the thermal time constant are important parameters that affect the performance, since they indicate how well the detector is isolated from the substrate and how fast the detector responses to the infrared radiation. The thermal simulations are implemented to simulate these parameters. The simulations are performed using the heat transfer module of the COMSOL Multiphysics program. Table 2.2 gives the physical parameters of the ZnO that are used in the thermal simulations. The parameters are taken from the COMSOL Multiphysics material database.

Table 2.2. Physical parameters of ZnO used in thermal simulations. The parameters are taken from the COMSOL Multiphysics material database.

Material	**Thermal Conductivity**	**Heat Capacity**	**Density**
ZnO	61.85 W/mK	505.73 J/kgK	5.67 gr/cm^3

In the simulations, the silicon substrate is adjusted to remain at a constant temperature as 300 K. A 100 nW heat is applied to the pixel body and the temperature variation of the detector area depending on time is observed. The temperature of the detector is initially set as 300 K. After the heat is applied, the detector temperature increases to reach a steady state value. The temperature variation characteristic is extracted from the simulation and the thermal conductance is obtained by,

$$G_{Th} = \frac{P_{applied}}{\Delta T} \tag{2.6}$$

where $P_{applied}$ represents the applied heat and ΔT is the temperature change. The time constant parameter is extracted from the heating curve of the detector.

Table 2.3 combines the results of the simulated thermal conductance and the extracted thermal time constant values of various pixels that have different arm and gap width values. Figure 2.6 gives the thermal simulation outcomes of a long-armed (pixel 6) and a short-armed pixel (pixel 33) that have the ZnO thickness of 450 nm and the cavity thickness of 1.6 µm.

From the results of the simulations, it is observed that the pixels that have long-armed geometry with an arm width and a gap width values of smaller than 1 µm have a thermal conductance value lower than 1.0×10^{-6}. They also have the time constant values in the range of 1.2-2.8 ms which means they are suitable for a 60 fps imaging system since the values are lower than 5 ms.

Table 2.3. Comparison of thermal simulation results of various pixels. The pixels that have long-armed geometry with the arm and the gap width values of smaller than 1 µm have a thermal conductance value lower than 1.0×10^{-6}, and a time constant value lower than 5 ms.

Pixel	Type	Arm width (µm)	Gap width (µm)	ΔT (K)	G_{Th} (W/K)	τ (ms)
Pixel 1	Type 1	0.5	0.5	0.200	5×10^{-7}	2.82
Pixel 6	Type 1	1	1	0.100	1.0×10^{-6}	1.20
Pixel 11	Type 1	1.5	1.5	0.060	1.6×10^{-6}	0.60
Pixel 16	Type 1	2	2	0.046	2.2×10^{-6}	0.39
Pixel 33	Type 2	1	1	0.013	7.7×10^{-6}	0.21

Pixel 6

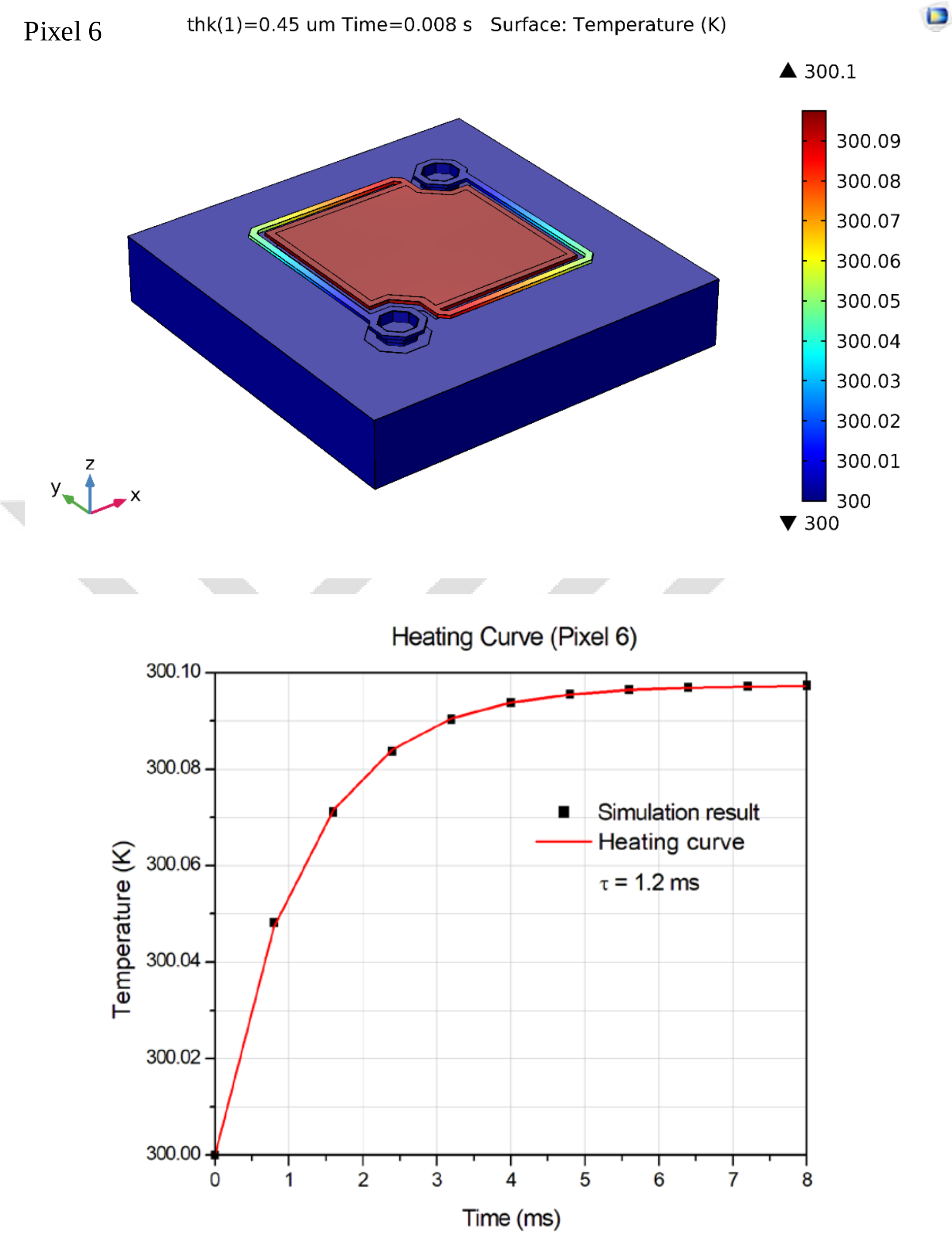

thk(1)=0.45 um Time=0.008 s Surface: Temperature (K)
▲ 300.1
300.09
300.08
300.07
300.06
300.05
300.04
300.03
300.02
300.01
300
▼ 300
z
y
x
Heating Curve (Pixel 6)
Temperature (K)
300.10
300.08
300.06
300.04
300.02
300.00
0
1
2
3
4
5
6
7
8
Time (ms)
Simulation result
Heating curve
τ = 1.2 ms

(a)

Pixel 33

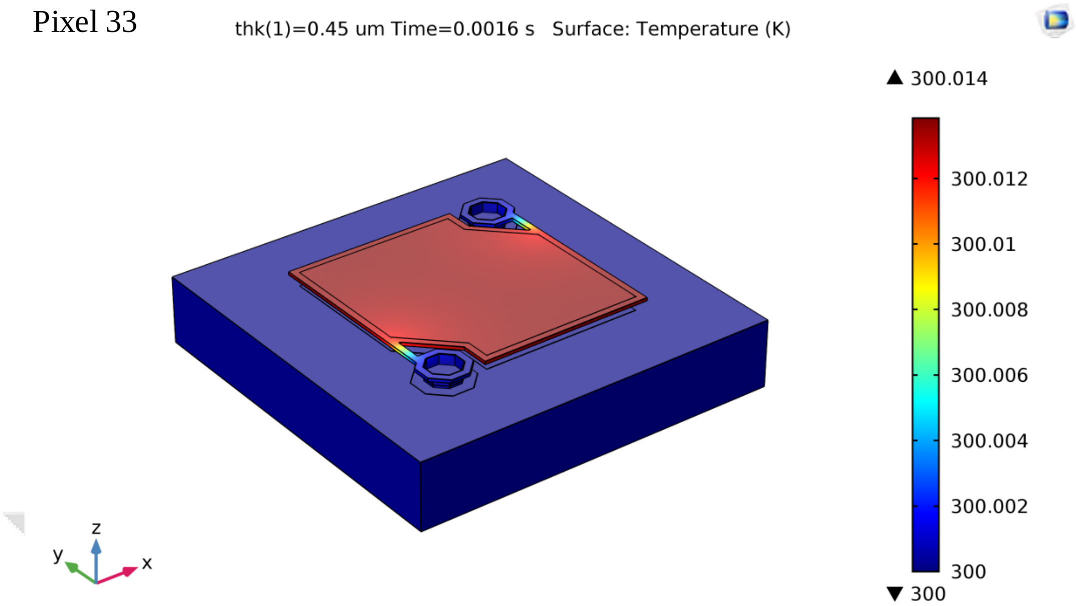

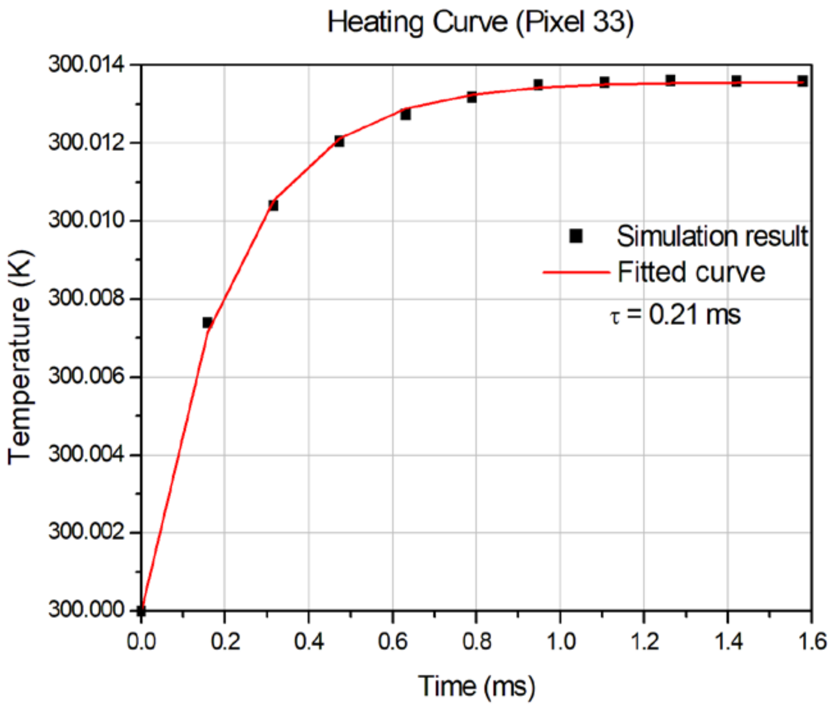

(b)

Figure 2.6. The thermal simulation outcomes of **(a)** a long-armed (pixel 6) and **(b)** a short-armed (pixel 33) pixel.

2.3.3. Mechanical Simulations

The mechanical simulations are performed to predict the mechanical durability of the detectors. As indicated before, the arm of the detectors should be strong enough to hold the suspended area without downfall to the substrate. The simulations are done by using solid mechanics module of the COMSOL Multiphysics software. In order to observe the motion of the suspended area caused by an outsourced force, 1000g acceleration is applied perpendicular to the pixel body while the position of the substrate and the anchor points are fixed. The Young's modulus and the Poisson ratio of the ZnO which are the required parameters to realize the mechanical simulations are taken from COMSOL material database as 210 GPa and 0.33, respectively.

Table 2.4 summarizes the mechanical simulation results of the various pixels that have the ZnO thickness of 450 nm and the cavity thickness of 1.6 µm while having different arm and gap width values. Figure 2.7 shows the simulation outputs of a long-armed (pixel 6) and a short-armed (pixel 33) pixel that are stated in the Table 2.4.

As can be seen from the results, the short-armed pixel has a maximum displacement of $8.2x10^{-4}$ µm against the applied acceleration. This value is smaller than the displacements of the long-armed pixel structures. When the long-armed pixels are compared with each other, it is seen that as the arm and the gap width values increase, the maximum displacement against the applied acceleration decreases. The maximum displacement of the pixel which has the smallest arm and gap width is $13.6x10^{-2}$ µm. By using these results, it is deduced that all of the pixels are strong enough to carry the suspended area not only in its stationary position but also when a shock is applied from the outside.

Table 2.4. Summary of the mechanical simulation results of the various pixels that have the ZnO thickness of 450 nm and the cavity thickness of 1.6 µm while having different arm and gap width values.

Pixel	Type	Arm width (µm)	Gap width (µm)	Max. displacement (µm)
Pixel 1	Type 1	0.5	0.5	$13.6x10^{-2}$
Pixel 6	Type 1	1	1	$5.2x10^{-2}$
Pixel 11	Type 1	1.5	1.5	$2.5x10^{-2}$
Pixel 16	Type 1	2	2	$1.3x10^{-2}$
Pixel 33	Type 2	1	1	$8.2x10^{-4}$

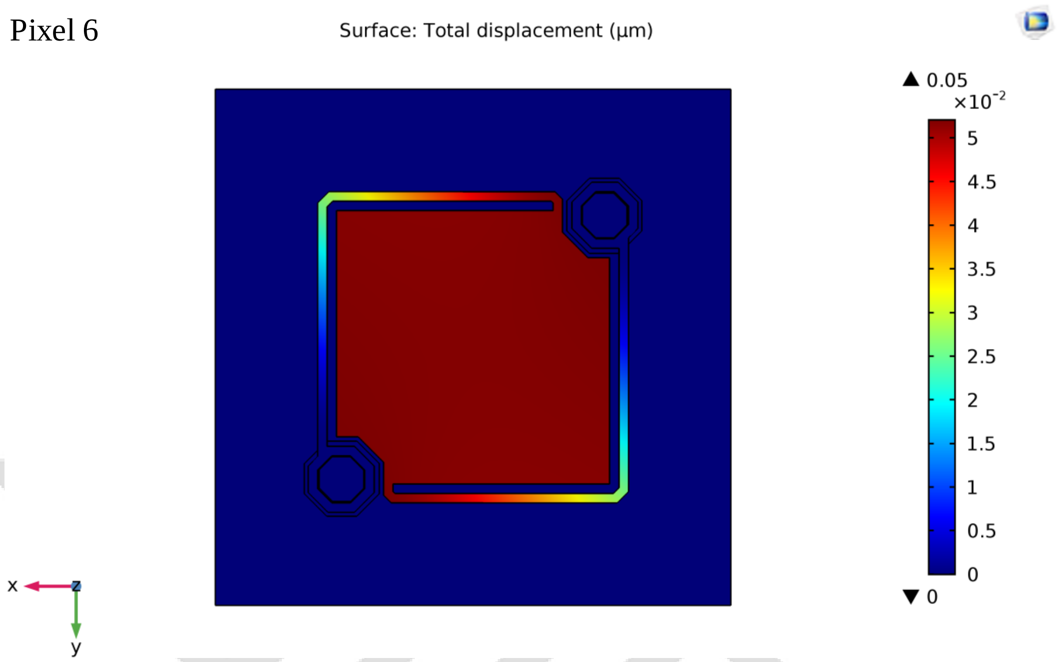

(a)

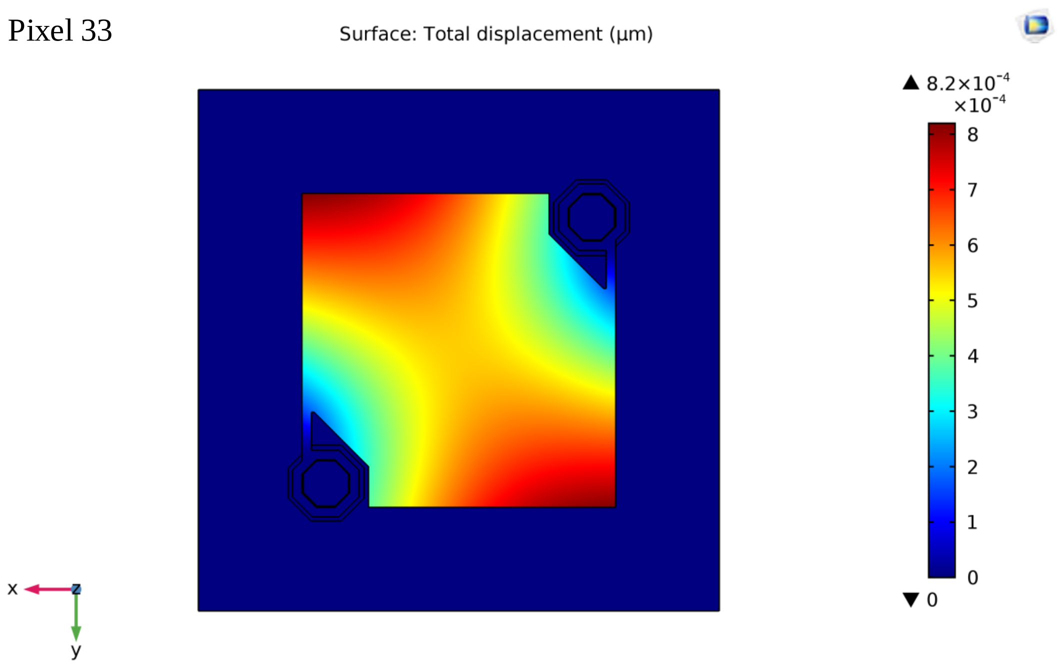

(b)

Figure 2.7. Mechanical simulation results of **(a)** a long-armed (pixel 6) and **(b)** a short-armed (pixel 33) pixel. Pixel 6 has a maximum displacement of $5.2\text{x}10^{-2}$ µm and pixel 33 has a maximum displacement of $8.2\text{x}10^{-4}$.

2.4. Conclusions

This chapter presents the design of a single layer microbolometer including the determination of the single layer material and the structural designs of the pixels that have variable geometric parameters. ZnO is selected as the single layer material and the pixel structures are categorized as Type 1 and Type 2 depending on their arm length.

The design parameters of the pixels are optimized by the optical, the thermal, and the mechanical simulations. The thermistor layer thickness and the cavity thickness parameters are optimized by using the optical simulations as 450 nm and 1.6 µm, respectively, with an average absorption rate of 83.5% in 8-12 µm wavelength range. Using these thickness values, the thermal and mechanical simulations are performed. It is seen that the short-armed pixels exhibit better mechanical strength and faster response but worse thermal isolation when compared with the long-armed pixels. However, the long-armed pixels that have the arm and the gap width values lower than 1 µm have the thermal conductance, the thermal time constant, and the mechanical strength values of the detectors that exhibit a moderate performance. Therefore, the long-armed pixel which has the arm and gap width values of 1 µm is chosen as the best structure since it has a thermal conductance of 1.0×10^{-6} W/K and a thermal time constant of 1.2 ms.

3. PROCESS OPTIMIZATION AND FABRICATION OF A SINGLE LAYER MICROBOLOMETER DETECTOR

This chapter explains the optimization of the process steps and fabrication of the single layer microbolometer detector pixels which are designed as in the previous chapter. Section 3.1 express the design of the fabrication process flow, section 3.2 states the optimization of the process steps individually, and section 3.3 gives the repeated simulation results of the revised single layer pixels through the process optimizations. In section 3.4, the results of the fabrication of the revised pixels are shared. Finally, section 3.5 summarizes all of the sections and concludes the chapter.

3.1. Design of the Fabrication Process

It is crucially important to apply the appropriate fabrication methods considering the requirements to construct the detector. There are many things that should be considered in the fabrication process of a microbolometer. The mirror material should be chosen to be a good reflector and also should be a good conductor since this material is also used in the connection pads between the microbridge and the readout circuitry. As mentioned in the previous chapter, gold is chosen to perform this task.

A sacrificial layer should be deposited between the mirror layer and the pixel area to give a cavity thickness as optimized in the pixel design stage. The coating and the etching processes of the sacrificial layer material should be CMOS compatible and should not have any negative effect on the entire pixel structure. Polyimide is selected to be used as the sacrificial layer since it is commonly used in the microstructures for this purpose, and it is also easy to fabricate (Bagolini et al., 2002; M. Yusuf Tanrikulu, 2007).

The deposition process of the single layer material directly affects the performance of the detector. Thus, the deposition method of the single layer should be selected to have high TCR, high optical absorption, and low stress. Atomic layer deposition method is preferred for deposition of the ZnO single layer since it is shown by the studies in the literature that the ALD deposited ZnO films provides the required properties.

Besides, allowing homogeneous deposition with the control of the film thickness plays an important role in making this decision.

A process that is composed of four steps is planned for the fabrication of a single layer microbolometer (Yildizak, Okyay, & Tanrikulu, 2017). Figure 3.1 shows the representative cross-sectional view of a single layer microbolometer detector pixel after each process step (M. Yusuf Tanrikulu et al., 2018). In the first step, the mirror layer and the contact pads are deposited and patterned (Figure 3.1 (a)). In the second step, the sacrificial layer is deposited and patterned to open the anchor points (Figure 3.1 (b)). In the third step, the single layer material is coated on to the sacrificial layer and patterned to be in form of a microbolometer (Figure 3.1 (c)). In the final step, the pixel structure comes out by etching the sacrificial layer (Figure 3.1 (d)). Figure 3.2 illustrates the 3D view of a single layer microbolometer detector pixel after each process step.

(a) After the deposition and the patterning of the mirror layer and the connection pads.

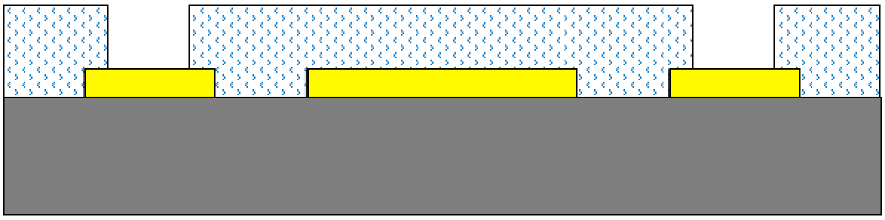

(b) After the deposition and the patterning of the sacrificial layer.

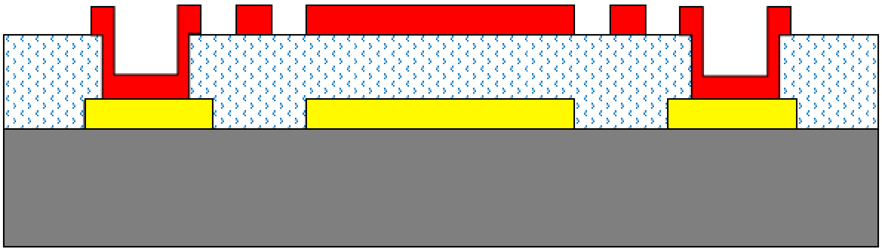

(c) After the deposition and the patterning of the single layer.

(d) After removal of the sacrificial layer and releasing the pixel.

Figure 3.1. Representative cross-sectional view of a single layer microbolometer detector pixel after each process step.

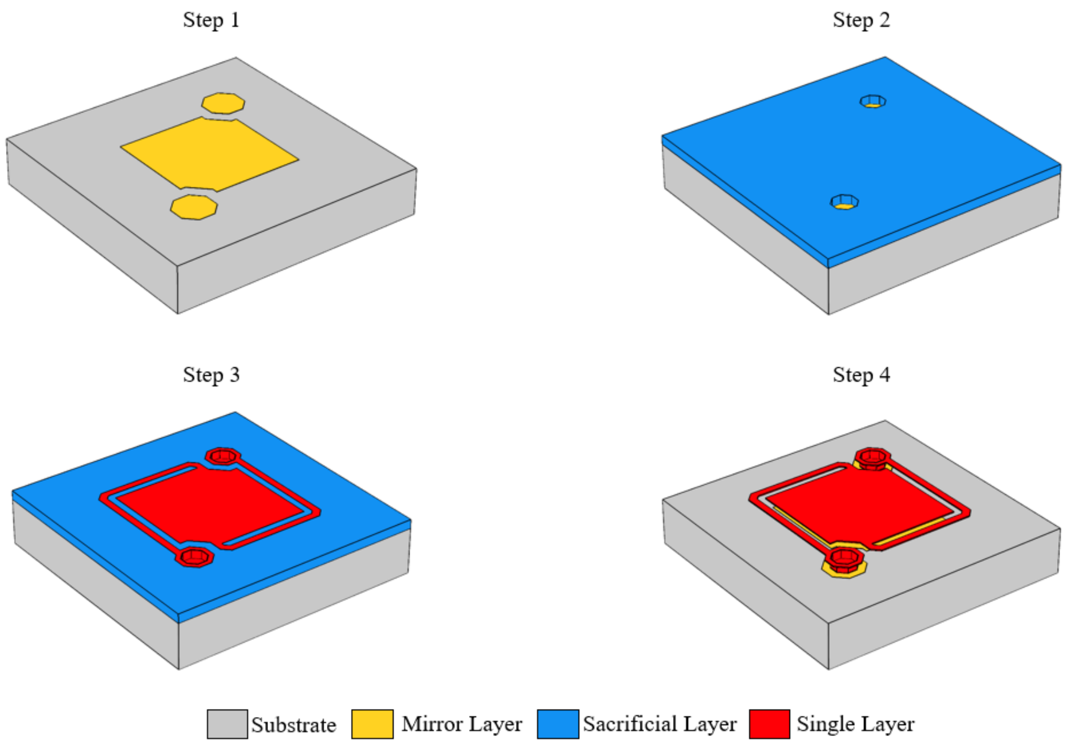

Figure 3.2. 3D view of a single layer microbolometer detector pixel after each process step.

The pixels are placed in a mask layout after the outline of the process steps is determined. All of the designed pixels are added to the mask in order to eliminate the problems in the fabrication steps. In case of facing a problem, the variety of pixels gives an opinion to the reason of the issue and helps to fix it easily. In the mask, the pad openings are placed nearby every single pixel for taking contact to perform inspections of the pixels. In addition to the single pixel layouts, little pixel arrays are also placed in the mask to perform optical measurements. Figure 3.3 shows the mask layout used in the fabrication process by focusing to show the layouts of sample pixels and small pixel arrays.

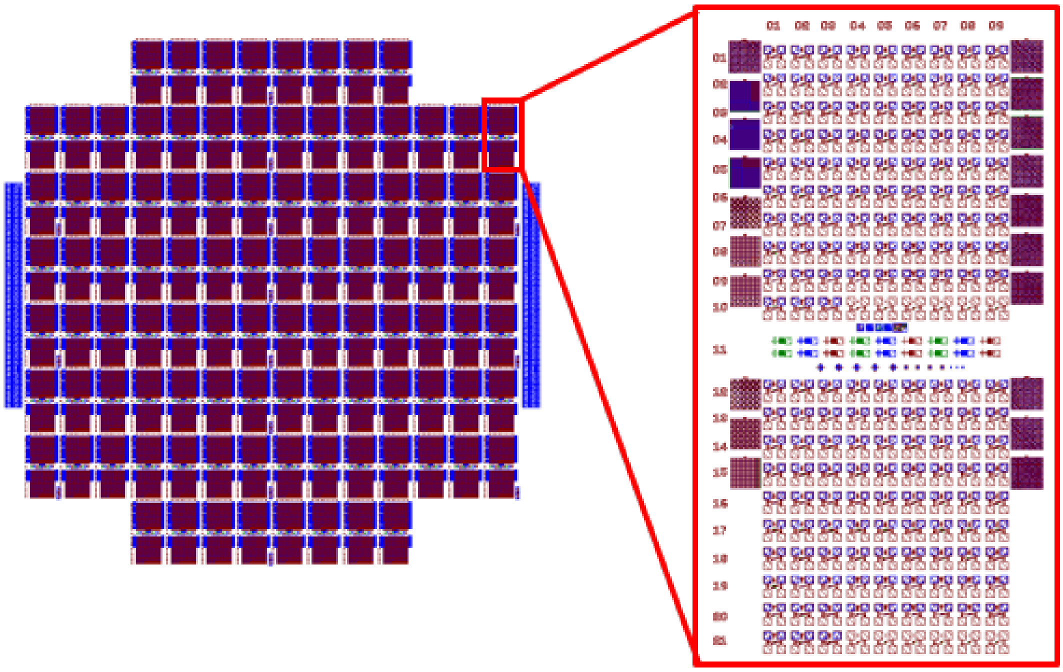

(a)

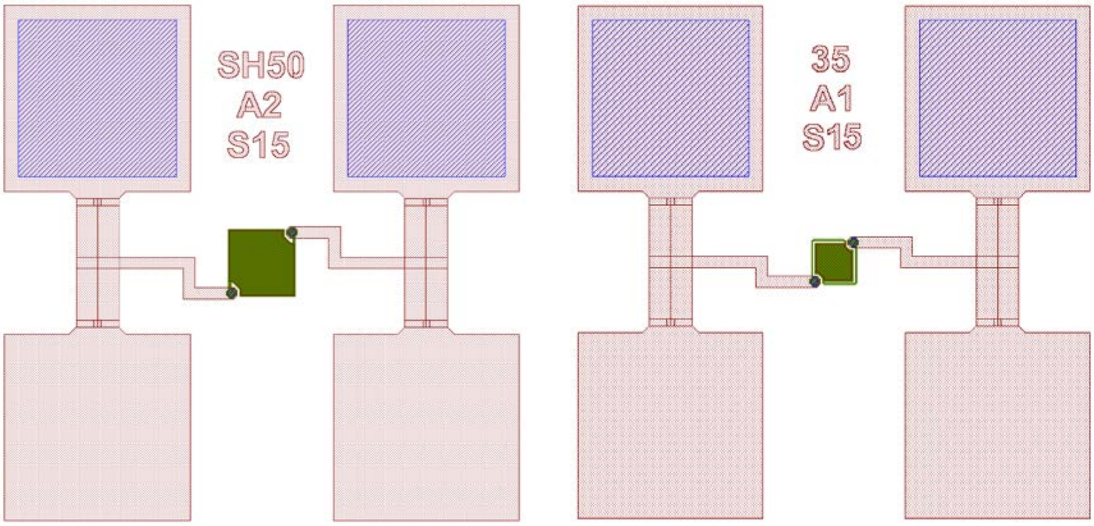

(b)

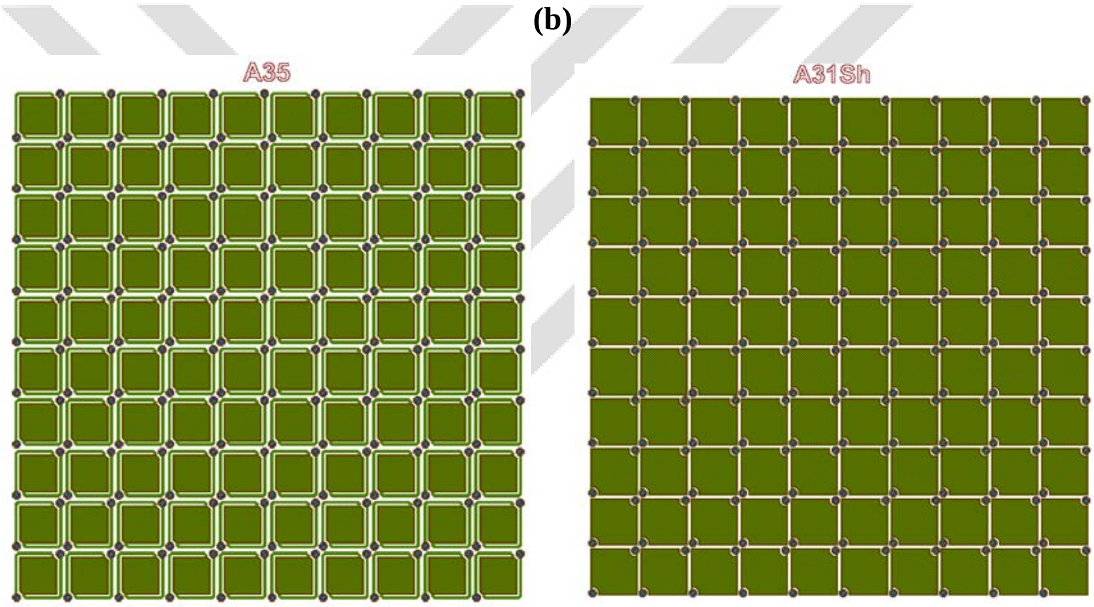

(c)

Figure 3.3. (a) The mask layout that is used in the fabrication process. **(b)** Sample layouts from the pixels that are used for pixel level test and optimization. **(c)** Sample layouts from the pixel arrays.

3.2. Optimization of the Process Steps

The process steps of the single layer microbolometer are optimized separately. Fabrication and optimization details of each step are explained in the following sections. The fabrication and optimization works are performed in METU MEMS Center.

3.2.1. Deposition and Patterning of Mirror Layer and Contact Pads

The fabrication process starts with the deposition and patterning of the mirror layer and the electrical connection pads. Gold is deposited on a nitride coated silicon substrate as the mirror layer and contact pads by sputtering method. A thin layer of titanium tungsten (TiW) is coated before the gold deposition to provide adhesion of gold to the substrate.

At first, patterning of the layer is performed by wet etching. However, since the wet etching results in undercut, reactive ion etching is used later instead of the wet etching process. Figure 3.4 shows the SEM images of the patterned mirror layer and electrical connection pads by using wet etching and reactive ion etching methods. As can be seen, the RIE process gives better results.

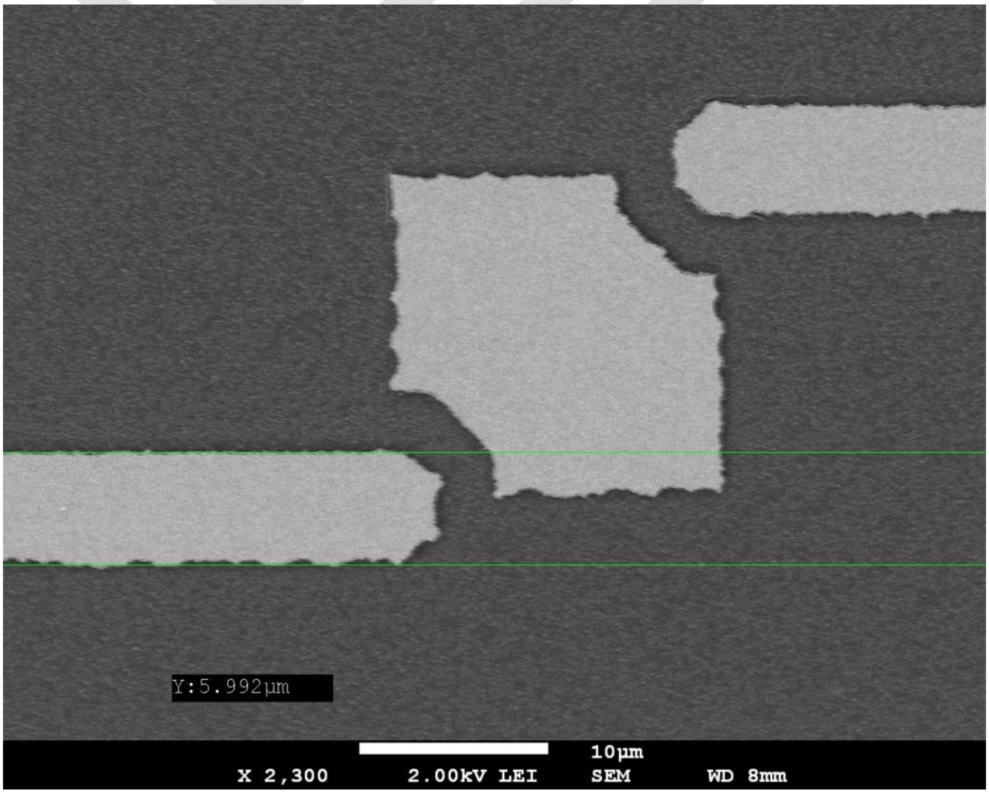

(a)

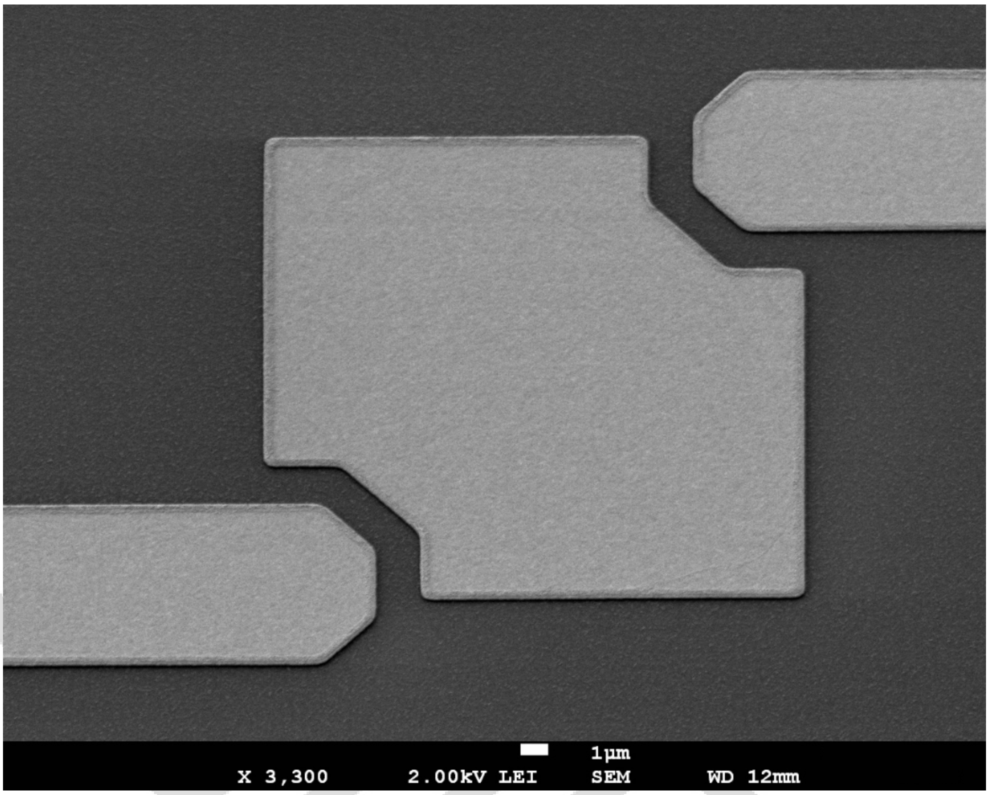

(b)

Figure 3.4. SEM images of the patterned mirror layer and electrical connection pads by using **(a)** wet etching and **(b)** reactive ion etching methods.

3.2.2. Deposition and Patterning of the Sacrificial Layer

The second step of the fabrication process is the deposition and patterning of the polyimide as the sacrificial layer. The deposition is performed by spin coating method. Coater speed is adjusted to have 1.6 µm thickness which is the optimized value of the cavity thickness to maximize the absorption.

In order to open the anchor points on the sacrificial layer, the layer is etched by reactive ion etching after using a titanium hard mask to prevent undercut. At the end of this step, the titanium hard mask is removed by wet etching. Figure 3.5 shows the SEM images of the successfully patterned sacrificial layer.

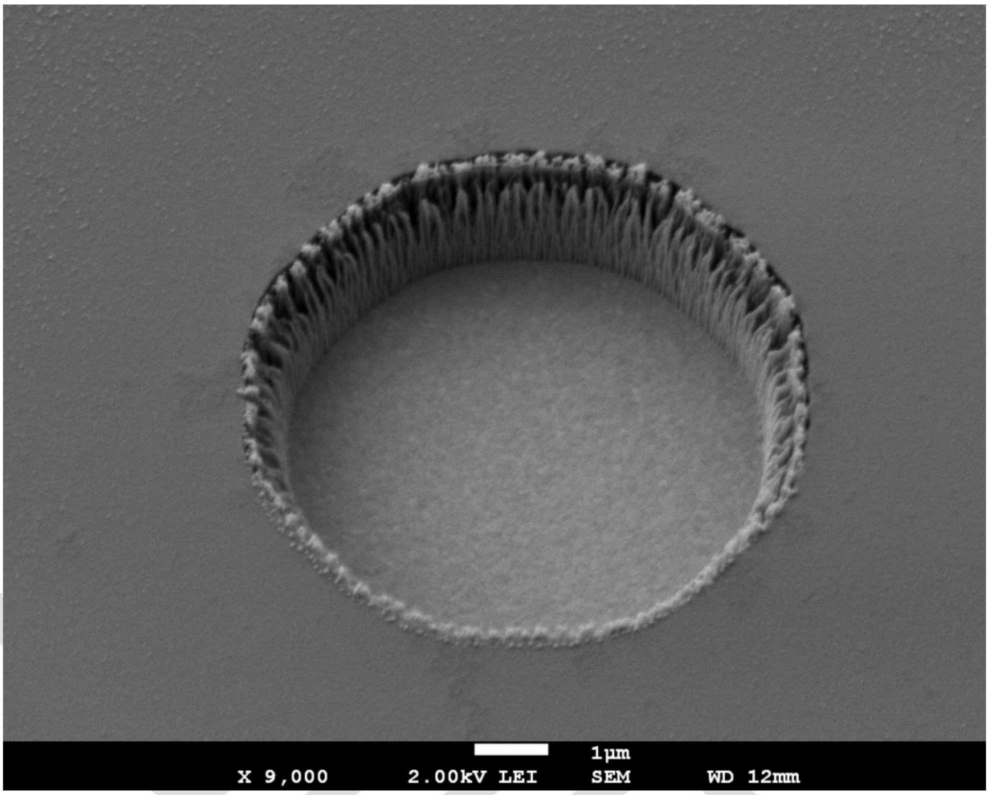

(a)

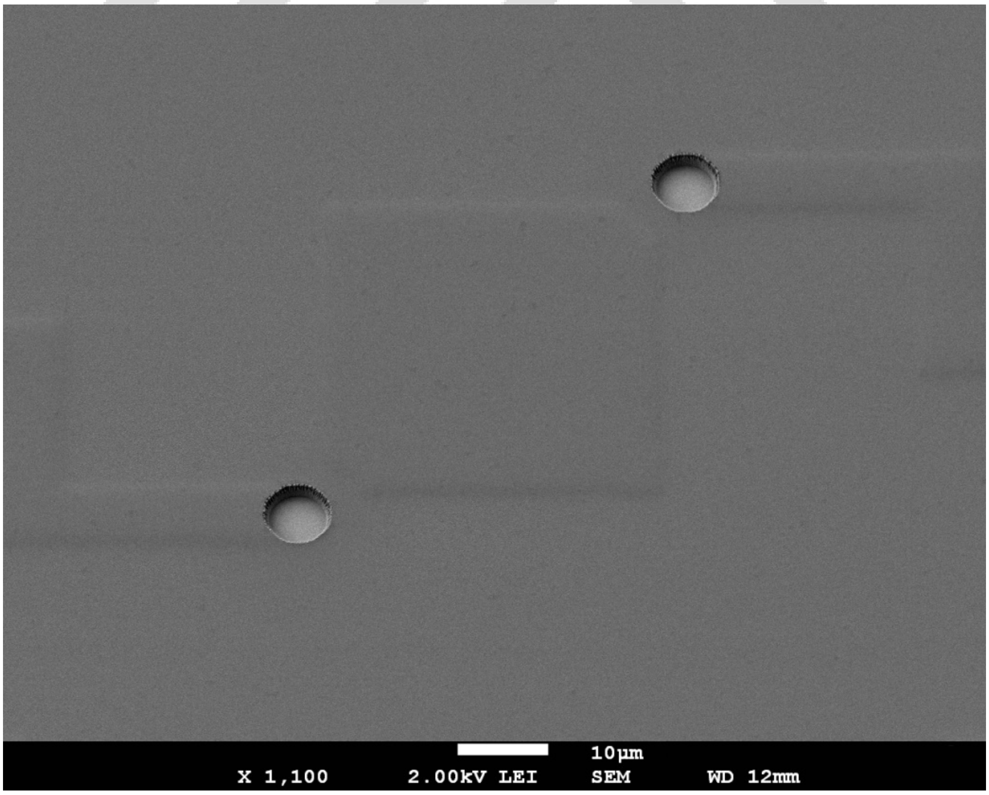

(b)

Figure 3.5. The SEM images of the successfully patterned sacrificial layer.

3.2.3. Deposition and Patterning of the ZnO Single Layer

Deposition of the ZnO is performed by atomic layer deposition method at 120°C since the films coated at this temperature have required properties of both an active material and absorber layer as mentioned previously. Diethylzinc (DEZ) and milli-Q water (H_2O) is used as reaction precursors during the process. The ZnO deposition process is performed in Okyay Tech.

After the ZnO film is coated, etching of the ZnO layer is started to pattern it to form as a pixel shape. The patterning process is pursued in the METU MEMS Center. Reactive ion etching method is used for etching since the wet etching method results in high undercut. In the etching trials, it is seen that the photoresist that used for patterning the layer is etched together with the ZnO. To solve this issue, the thickness of the photoresist is increased, but this time, the residues of the ZnO accumulated on the edge of the photoresist during the etching process. Therefore, decreasing the ZnO thickness instead of increasing the photoresist thickness becomes a necessity.

The thickness of the ZnO is decreased down to 25 nm and patterning of the ZnO with this thickness is achieved. Figure 3.6 shows the successfully patterned ZnO layer in the pixel shapes of Type 1 and Type 2.

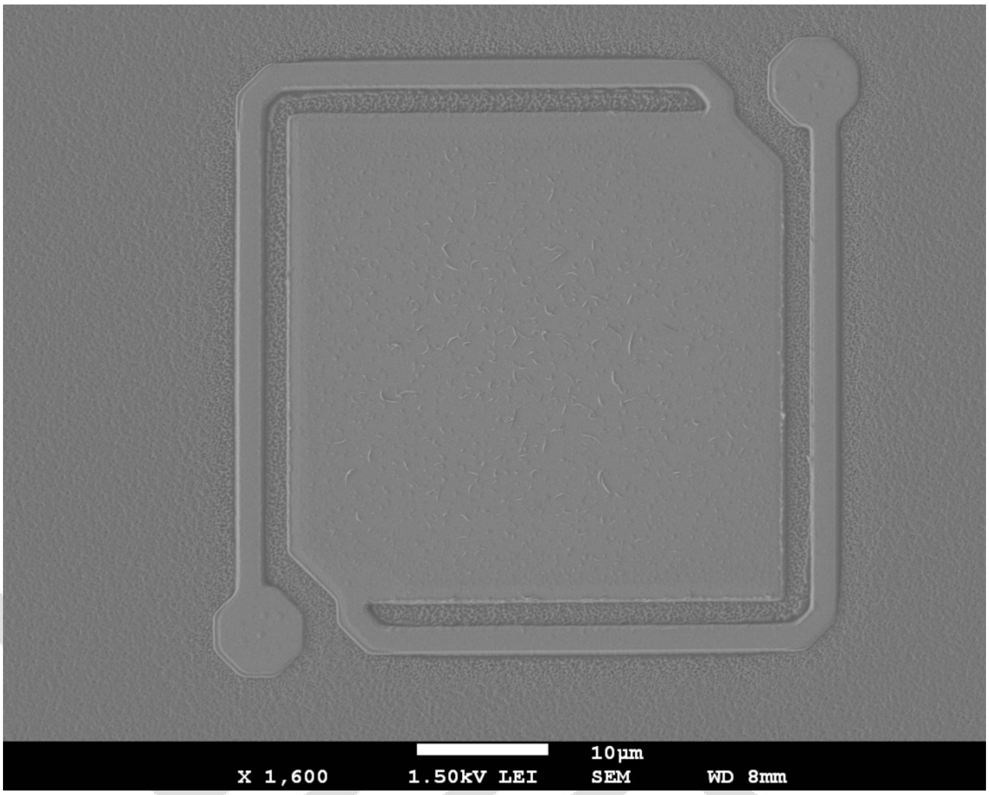

(a)

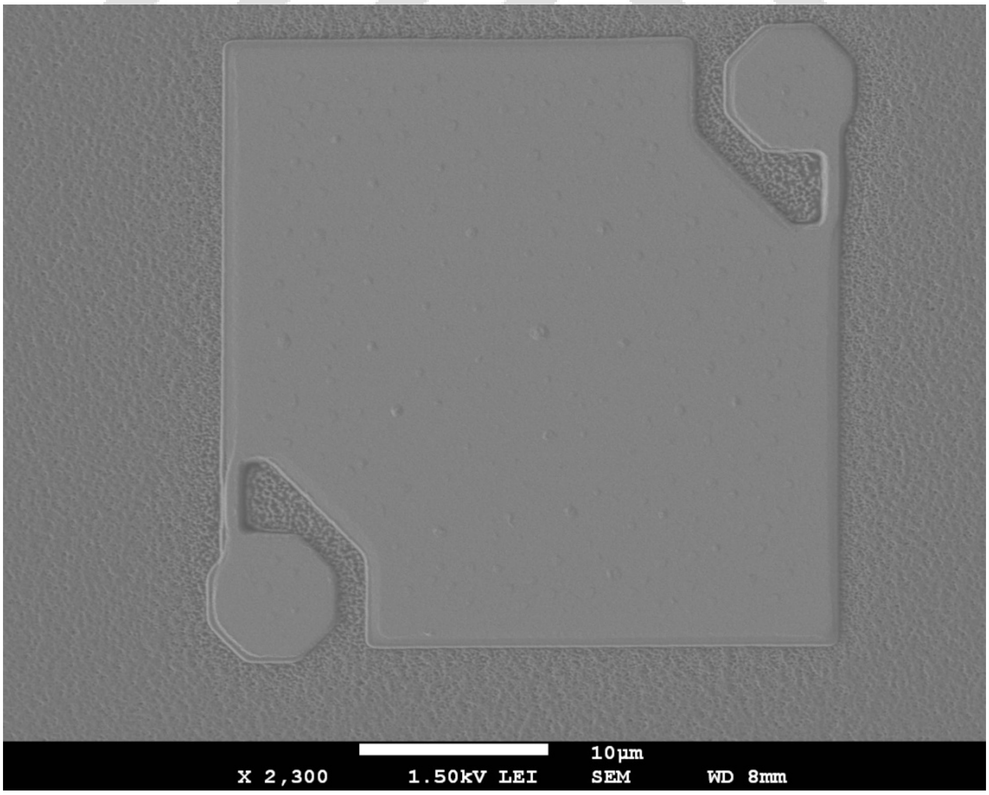

(b)

Figure 3.6. The successfully patterned ZnO layer in the pixel shapes of **(a)** Type 1 and **(b)** Type 2.

3.3. Revision of the Pixel Designs by Fabrication Optimizations

Decreasing the thickness of the ZnO layer due to the fabrication processes directly affects all of the performance parameters. In order to see the results of this decreasing effect, the optical, thermal, and mechanical simulations are repeated. The details are given in the subsections below.

3.3.1. Optical Properties of the Revised Pixels

The optical simulations are repeated to find the new cavity thickness value to maximize the absorption for the new ZnO thickness which is obtained at the results of the process optimizations as 25 nm. It is seen at the results of the simulations that the cavity thickness should be 2.2 µm to maximize the absorption. The average absorption in the 8-12 µm wavelength range is extracted as 9.9% by using the values of the ZnO and cavity thickness as 25 nm and 2.2 µm, respectively. Figure 3.7 shows the results of the repeated optical simulations.

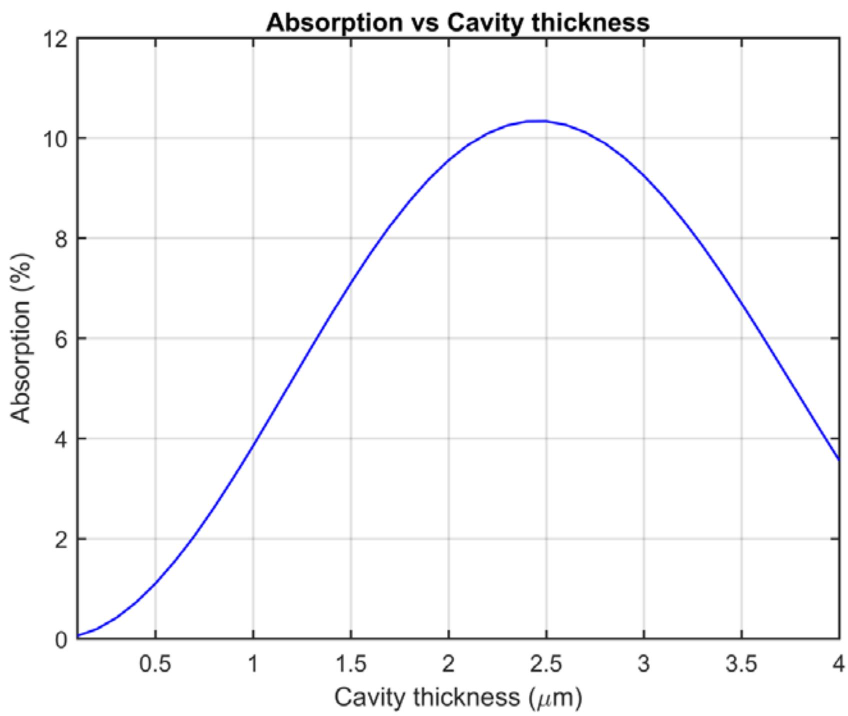

(a)

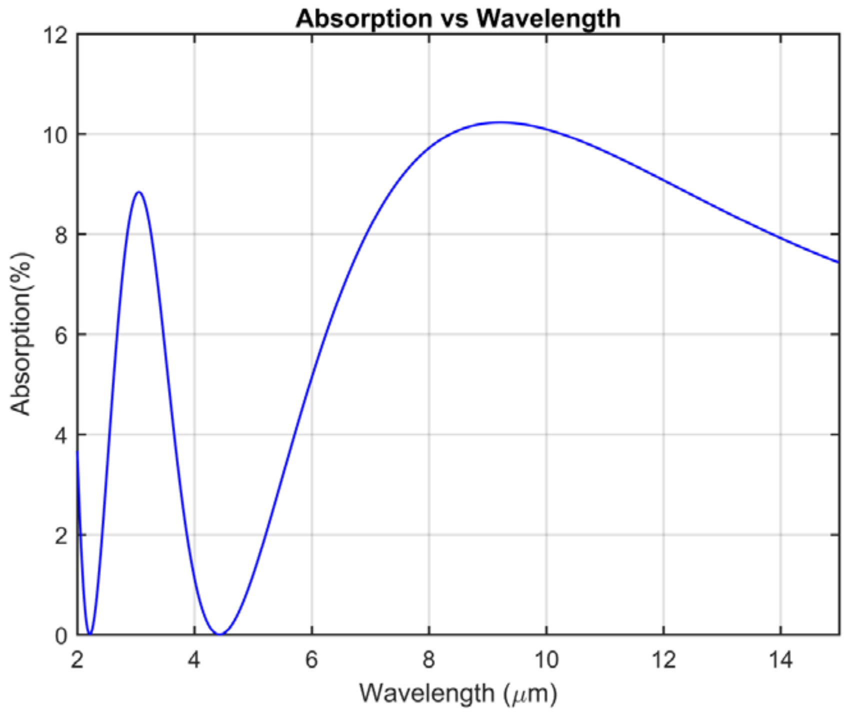

(b)

Figure 3.7. Optical simulations of revised pixels. **(a)** The new cavity thickness corresponding to 25 nm ZnO thickness is found as 2.2 µm and **(b)** the average absorption in the 8-12 µm wavelength range is extracted as 9.9%.

3.3.2. Thermal Properties of the Revised Pixels

The thermal simulations that are detailed in Chapter 2 are repeated in this part to see the effects of process optimizations on the thermal conductance and the thermal time constant parameters. Figure 3.8 shows the repeated thermal simulation results of Type 1 and Type 2 pixels.

Table 3.1 summarizes the repeated thermal simulation results for the ZnO thickness of 25 nm and the cavity thickness of 2.2 µm. In the results, it is seen that the decrease in the ZnO thickness decreases also the thermal conductance and increases the thermal time constant. Despite the thermal time constants of the pixels increase, they are still lower than 5 ms, which means they are still suitable for a 60 fps imaging system.

Table 3.1. Repeated thermal simulation results for the ZnO thickness of 25 nm and the cavity thickness of 2.2 µm.

Pixel	**Type**	**Arm width (µm)**	**Gap width (µm)**	**ΔT (K)**	**G_{Th} (W/K)**	**τ (ms)**
Pixel 1	Type 1	0.5	0.5	3.55	0.28×10^{-7}	3.88
Pixel 6	Type 1	1	1	1.73	0.58×10^{-7}	1.62
Pixel 11	Type 1	1.5	1.5	0.89	1.12×10^{-7}	0.81
Pixel 16	Type 1	2	2	0.80	1.25×10^{-7}	0.48
Pixel 33	Type 2	1	1	0.21	4.76×10^{-7}	0.24

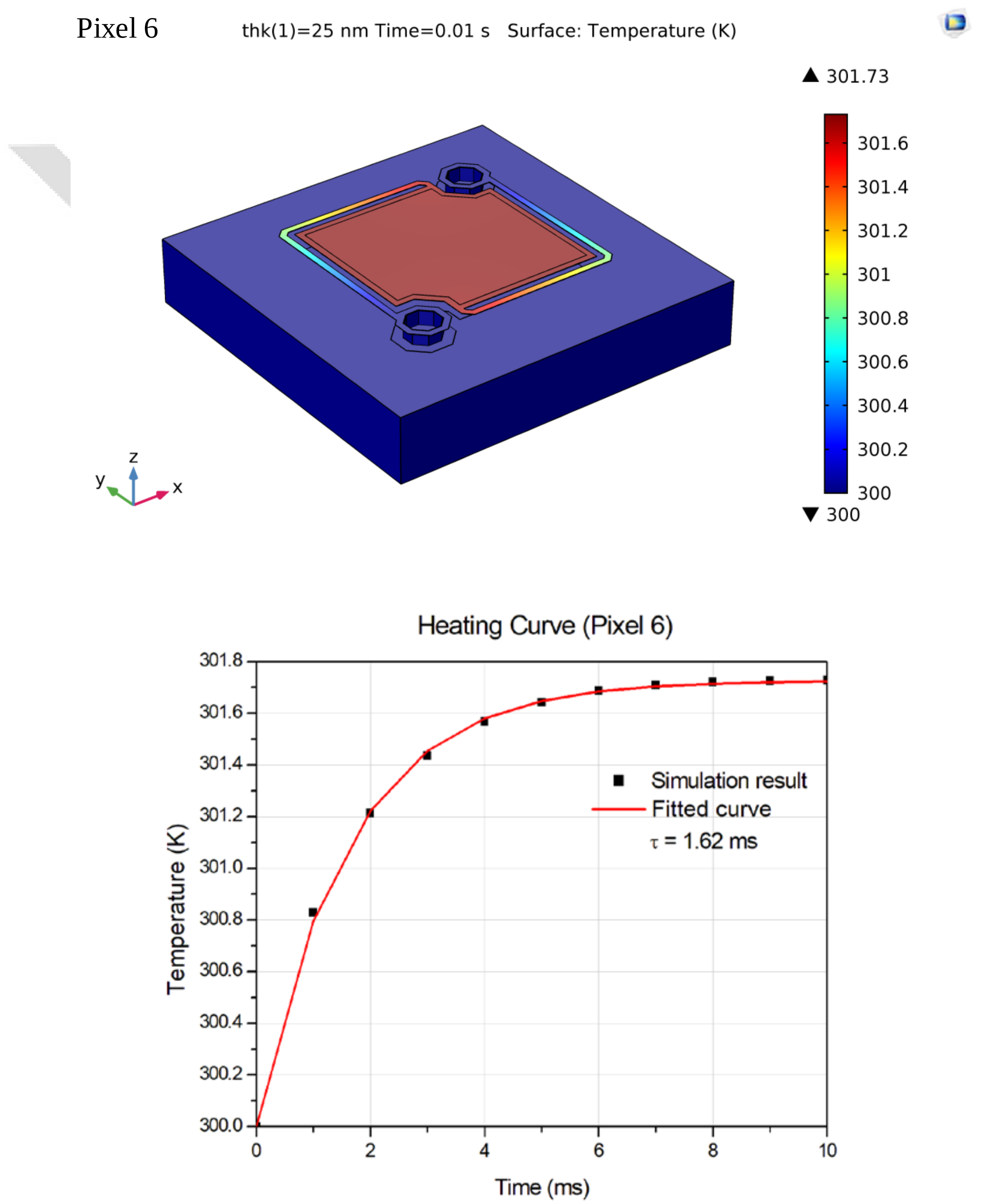

(a)

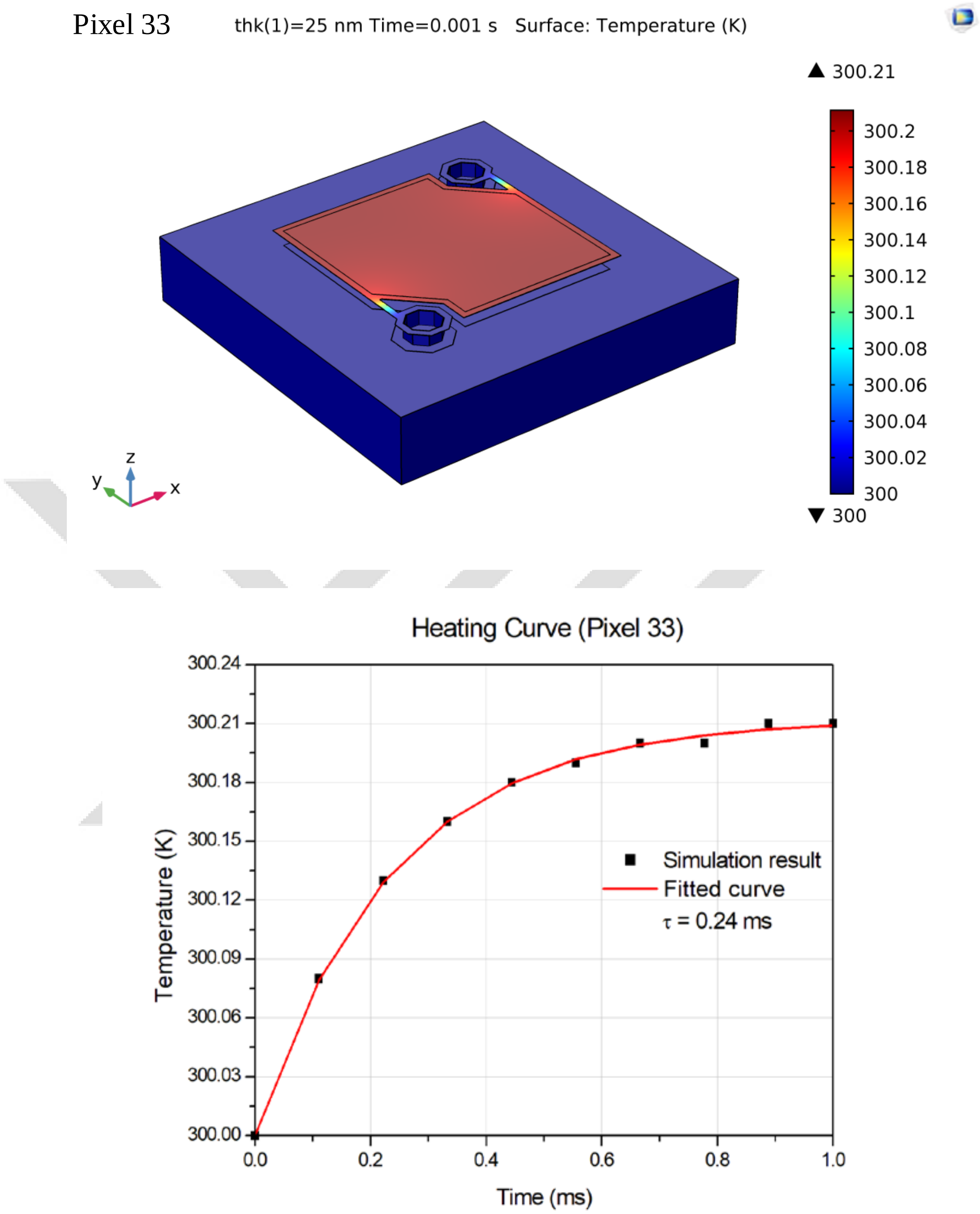

(b)

Figure 3.8. Repeated thermal simulation results of **(a)** Type 1 (pixel 6) and **(b)** Type 2 (pixel 33) pixels.

3.3.3. Mechanical Properties of the Revised Pixels

The mechanical simulations are repeated to investigate the effect of thinner ZnO single layer on the durability of the pixel. Table 3.2 gives the repeated mechanical simulation results for 25 nm ZnO and 2.2 µm cavity thicknesses. In the simulations, it is observed that the Type 1 pixels are not strong enough when a 1000g external acceleration is applied. For this type of pixels, the simulations are performed by applying 100g and it is seen that the pixels that have an arm and a gap width values higher than 1 µm have a maximum displacement value lower than the cavity thickness value of 2.2 µm. It means these pixels can preserve their suspended form without falling on to the substrate when 100g is applied.

When the Type 2 pixels are simulated, it is seen that this type of pixels have a stronger mechanical structure than the Type 1 pixels since their maximum displacement values are reasonable when 1000g of an external acceleration is applied.

Table 3.2. Repeated mechanical simulation results for 25 nm ZnO and 2.2 µm cavity thicknesses.

Pixel	Type	Arm width (µm)	Gap width (µm)	Acceleration (m/s^2)	Max. displacement (µm)
Pixel 1	Type 1	0.5	0.5	100g	4.68
Pixel 6	Type 1	1	1	100g	1.69
Pixel 11	Type 1	1.5	1.5	100g	0.81
Pixel 16	Type 1	2	2	100g	0.38
Pixel 33	Type 2	1	1	100g	0.02×10^{-2}
Pixel 16	Type 1	2	2	1000g	3.76
Pixel 33	Type 2	1	1	1000g	0.24

3.4. Release of the Single Layer Microbolometer Pixel

After all of the process steps are optimized individually, the steps are combined to conclude the fabrication of a single layer microbolometer pixel. Deposition and patterning of the mirror layer, sacrificial layer, and ZnO thermistor layer are realized successfully. But in the last process step which is the removal of the sacrificial layer, various problems were encountered. The fabricated wafer is inspected by taking the sample dies from various positions. Figure 3.9 shows the numerated die map of the fabricated 8” wafer.

Figure 3.10 gives the optical microscope views of the pixels in the die #221, after the removal of the sacrificial layer. It is observed that there are some residues in the field around the pixels. It is thought as the reason of this issue that the etching of the ZnO is not completed exactly and in the step of the removal of the sacrificial layer, the etchant leaks from the fractures of the remained ZnO layer to the sacrificial layer. When the etchant reaches to the sacrificial layer, it etches the layer and causes the remained ZnO residues to fall down to the substrate as appear in Figure 3.10 (a). This case can be better observed by the SEM views of the pixels as in Figure 3.10 (b) and (d).

Another issue is that etching of the sacrificial layer is not completed exactly in some areas, especially in the pixels which have 50 µm pitch. It is observed that in the middle area of these pixels the polyimide remains as can be seen in the Figure 3.10 (b) and (c).

As going through the edges of the wafer, it is seen that there are no residues in the field around the pixels. However, this time another problem shows up. In the dies stated near the edge of the wafer, the arms or the body of the pixels are etched partially or completely. Figure 3.11 gives the optical microscope views of the dies #175 and #179 which are near the edge of the wafer.

It is deduced that the layers coated on the wafer have non-uniform thickness values throughout the wafer since the release process show different characteristics between the dies in the middle of the wafer and at the edge of the wafer. Although there are many problems due to this thickness non-uniformity, pixels and arrays are successfully released at the end of the fabrication process. Figure 3.12 shows SEM images of the successfully released pixels. It is seen that there is buckling on the released pixels. A possible reason for this situation is the process temperature of the removal of the sacrificial layer.

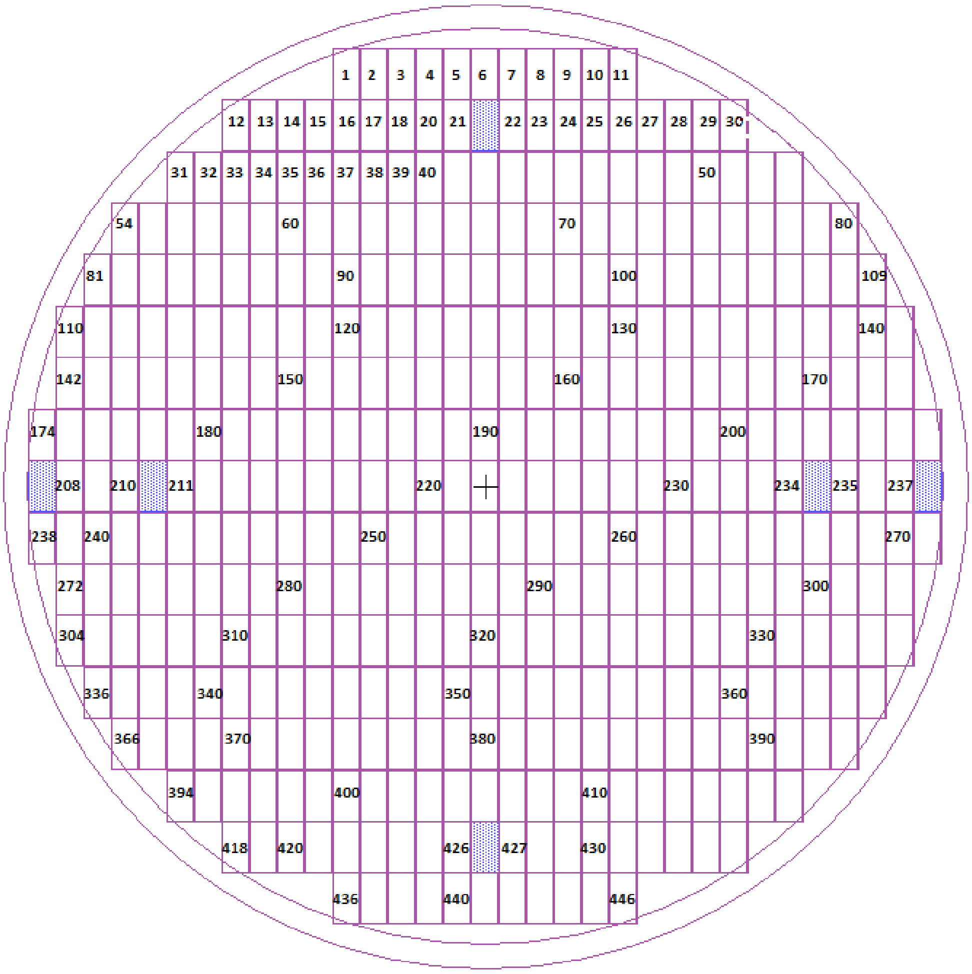

Figure 3.9. Numerated die map of the fabricated 8” wafer.

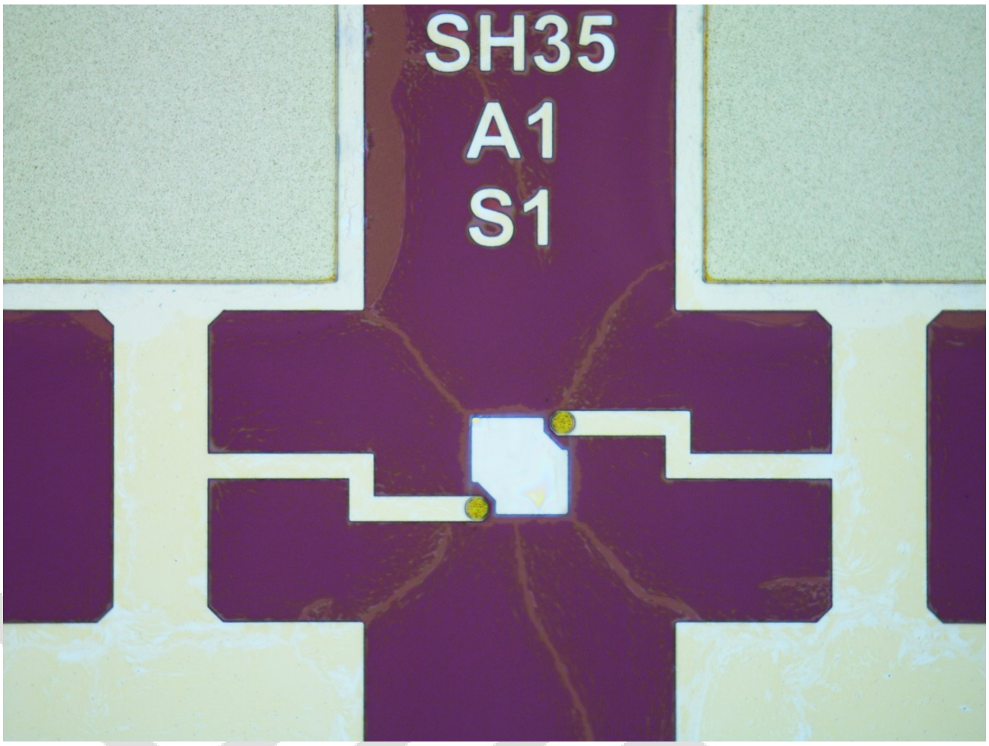

(a)

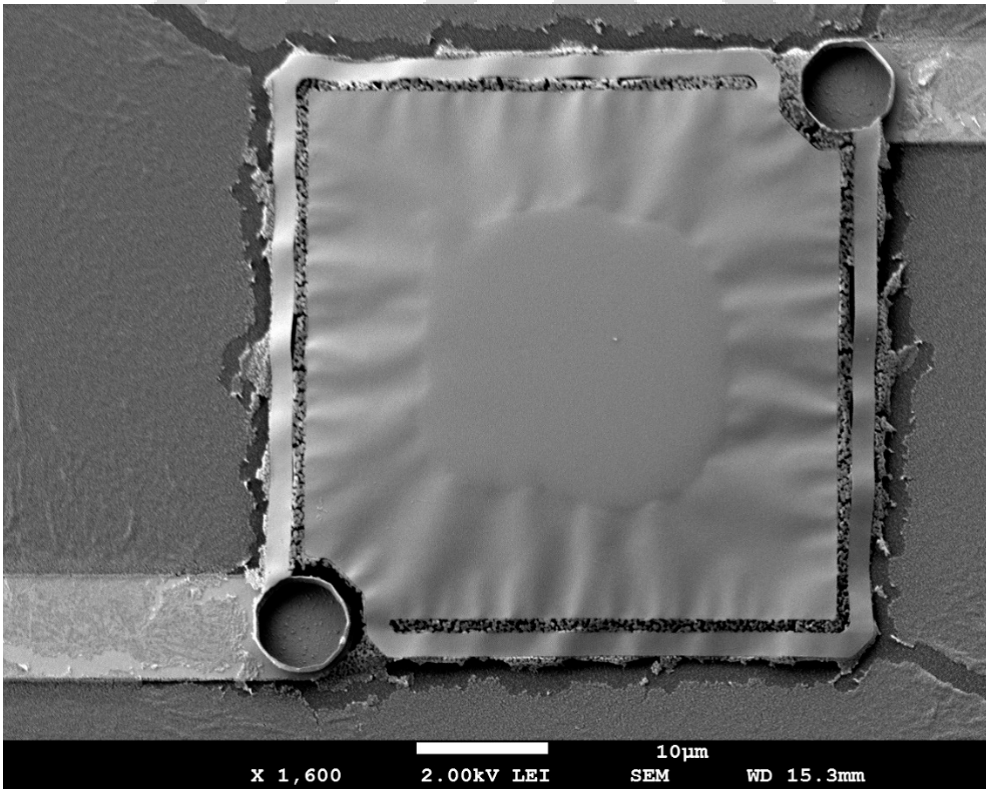

(b)

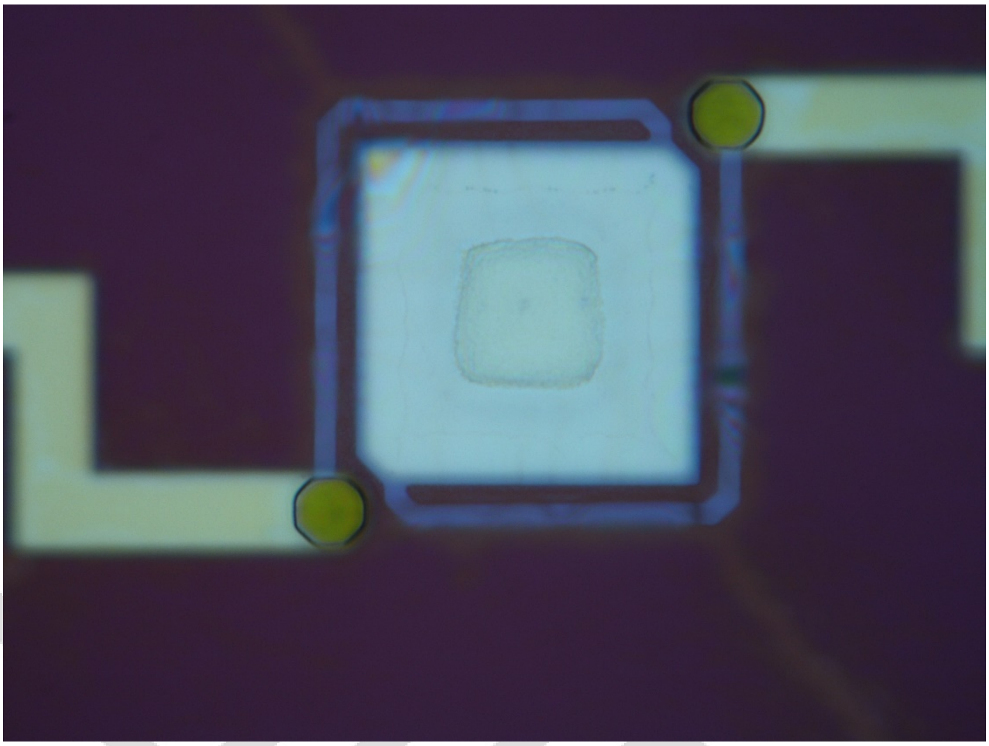

(c)

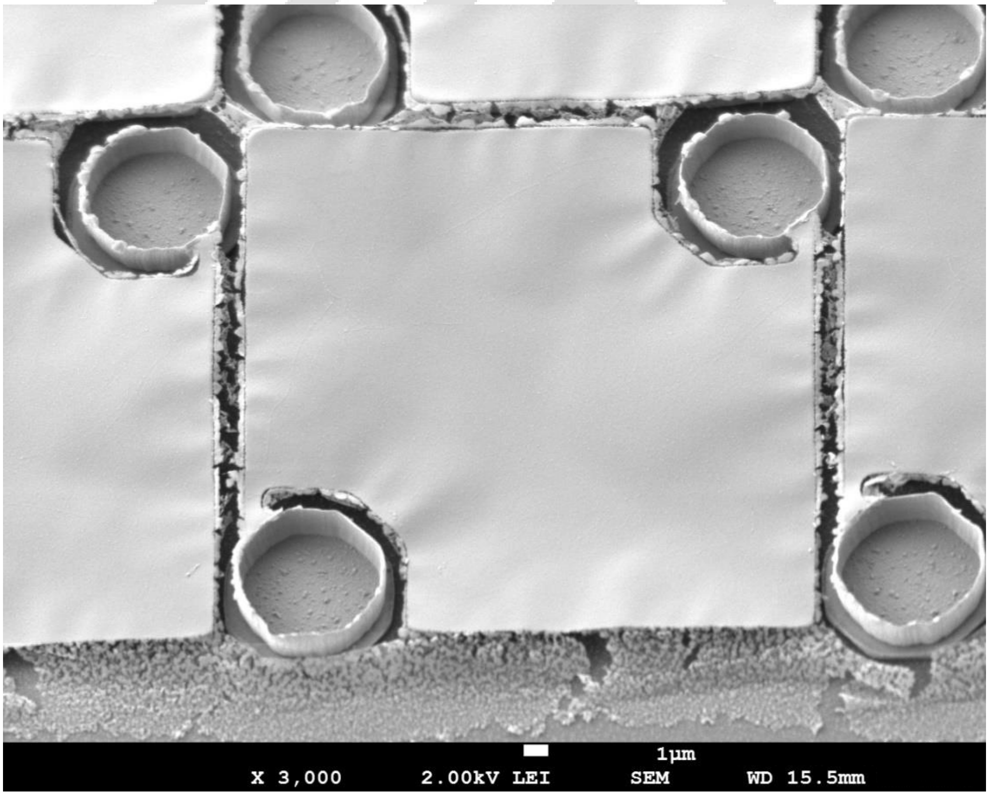

(d)

Figure 3.10. Optical microscope and SEM views of the pixels in the die #221, after the removal of the sacrificial layer.

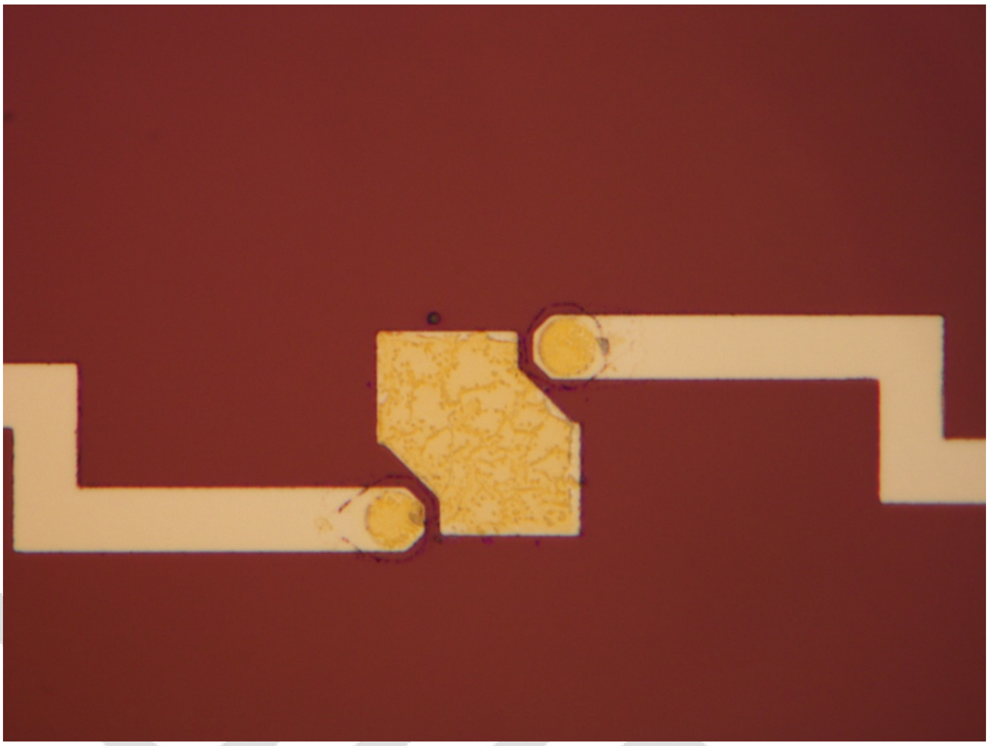

(a)

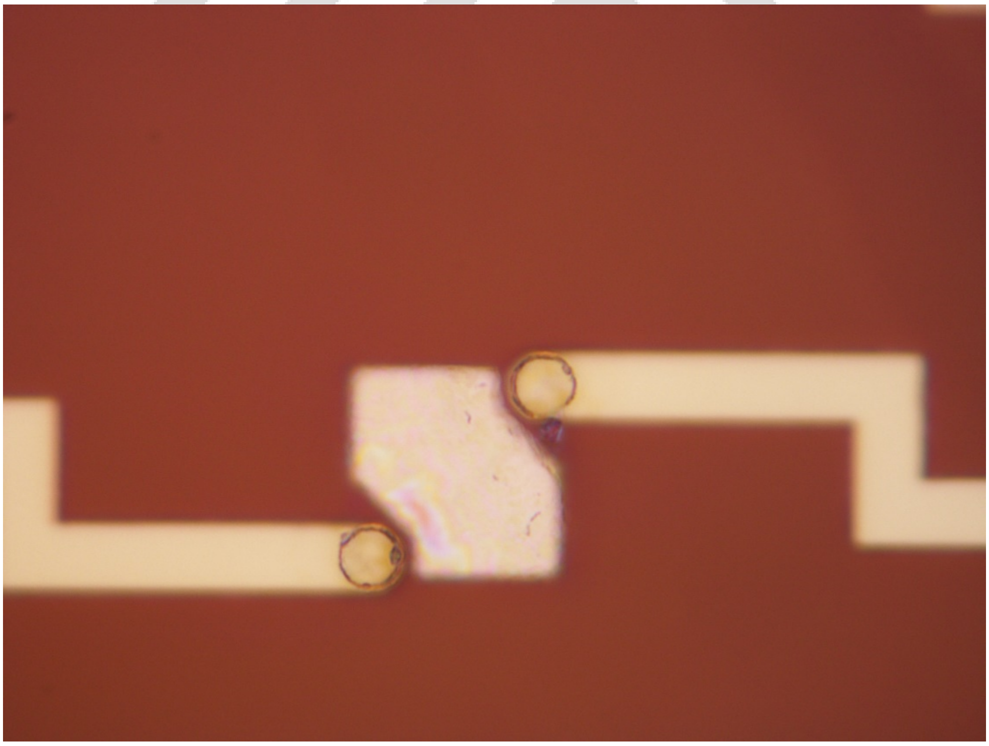

(b)

Figure 3.11. Optical microscope views of the pixels from dies of #175 and #179 which are near the edge of the wafer.

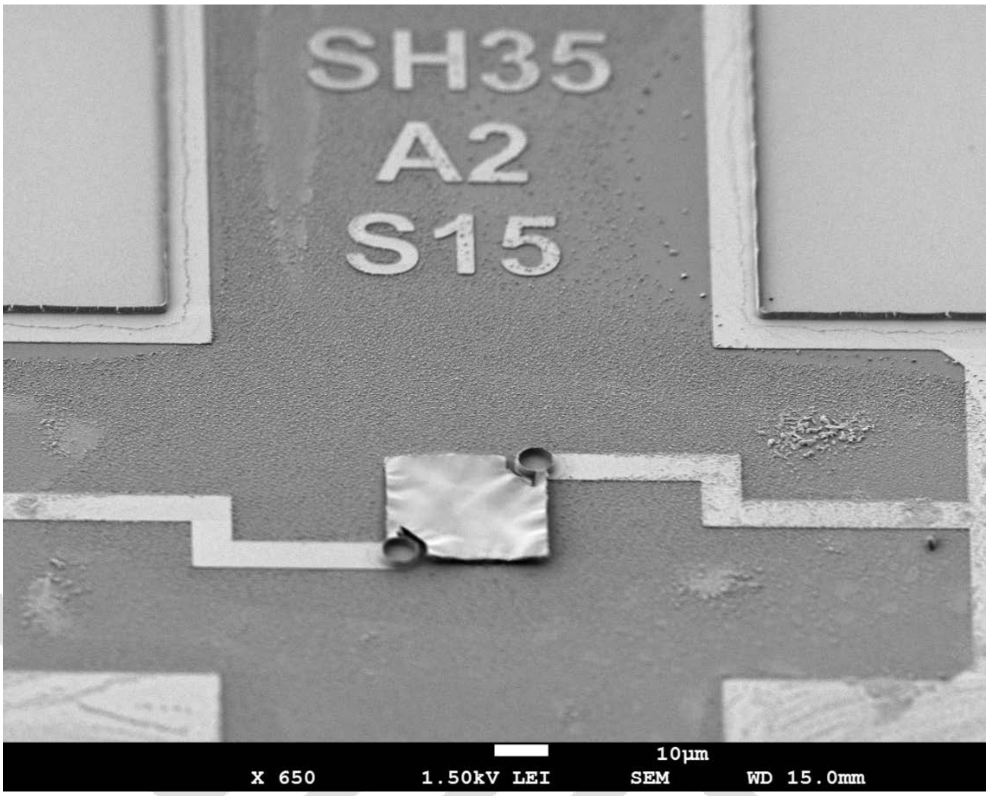

(a)

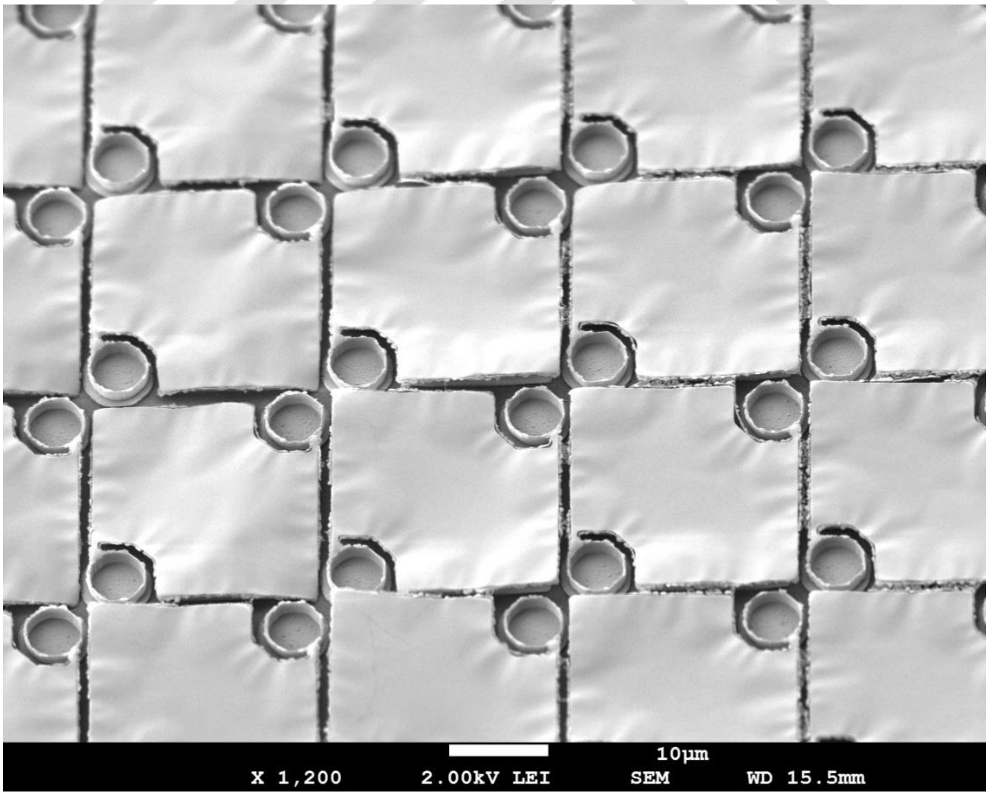

(b)

Figure 3.12. Samples of successfully released pixels.

3.5. Conclusion

This chapter presents a four-step process for the fabrication of a single layer microbolometer detector. The steps are specified as deposition and patterning of the mirror layer, sacrificial layer, and thermistor layer, and removal of the sacrificial layer. All of the steps are optimized individually and results are shared.

At the end of the optimization studies, it is seen that the ZnO thickness of 450 nm is not applicable due to process limitations. Therefore, the thickness of the ZnO is reduced to 25 nm, and the corresponding cavity thickness is extracted as 2.2 µm by repeating the optical simulations. In this new case, the infrared absorption amount is simulated as 9.9% which is quite low.

The thermal and mechanical characteristics of the revised pixels are also investigated by repeating the thermal and mechanical simulations. At the results of the repeated thermal simulations, the thermal conductance decreases and the thermal time constant increases. In order to the thermal time constants of the simulated pixels are still lower than 5 ms, they are still suitable for a 60 fps imaging system. Along with the decreasing the thermal conductance values of the detectors, all of the pixels provide the requirement of a common microbolometer. At the results of the repeated mechanical simulations, it is seen that the Type 1 pixels are not durable to 1000g external acceleration while the Type 2 detectors are durable. The maximum displacement of a simulated Type 2 pixel is obtained as 0.24 µm when 1000g acceleration is applied. The simulations of the Type 1 detectors are repeated by applying 100g and it is seen that only the pixels that have an arm and a gap width value higher than 1 µm are durable to this acceleration. In summary, decreasing the thickness of the ZnO layer decreases the performance of the detector.

After the optical, thermal, and mechanical properties of the revised detectors are investigated, the fabrication process steps are combined to conclude the pixel production. The fabrication is proceeded up to the last step without any problem. However, in the last step, many problems show up related to the non-uniformity of the coated wafer. Even so, successfully released pixels are also obtained.

4. TESTS OF THE FABRICATED SINGLE LAYER MICROBOLOMETER DETECTORS

In this chapter, the tests of the fabricated single layer microbolometer detector pixel are presented. TCR, noise, and optical measurements are detailed in the sections below.

4.1. TCR Measurement

TCR is one of the most important parameters that indicate the performance of a microbolometer as mentioned in the previous chapters. TCR measurement of a ZnO resistor that is grown by the atomic layer deposition method at 120 °C is performed by using a measurement setup as shown in Figure 4.1. The setup includes a cold/hot plate, a microscope camera, a manipulator, probes, a sourcemeter, a power supply, a multimeter, and a computer.

During measurements, a constant current of 5 μA is applied to the resistor which is placed on to the cold/hot plate. Then the temperature of the cold/hot plate is changed between 18-28 °C. The voltage on the resistor is measured by using a multimeter, while the temperature of the cold/hot plate is measured by a sensor (AD590LF).

The measured resistance depending on the temperature is analyzed in the computer environment. The graph of the resistance change characteristic is drawn and fitted on a polynomial function. The extracted resistance function is used in Equation (1.7) and the function of the TCR is obtained. Figure 4.2 gives the graphs of the resistance and the TCR variation depending on the temperature. As seen, the TCR reaches its maximum value around 20 °C as -10.5 %/K. The results are consistent with the values reported in the literature (Battal et al., 2014).

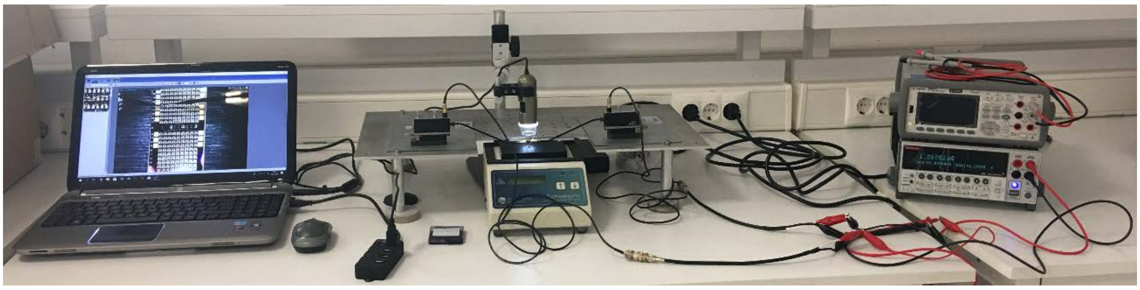

Figure 4.1. The TCR measurement setup. The setup includes a cold/hot plate, a microscope camera, a manipulator, probes, a sourcemeter, a power supply, a multimeter, and a computer.

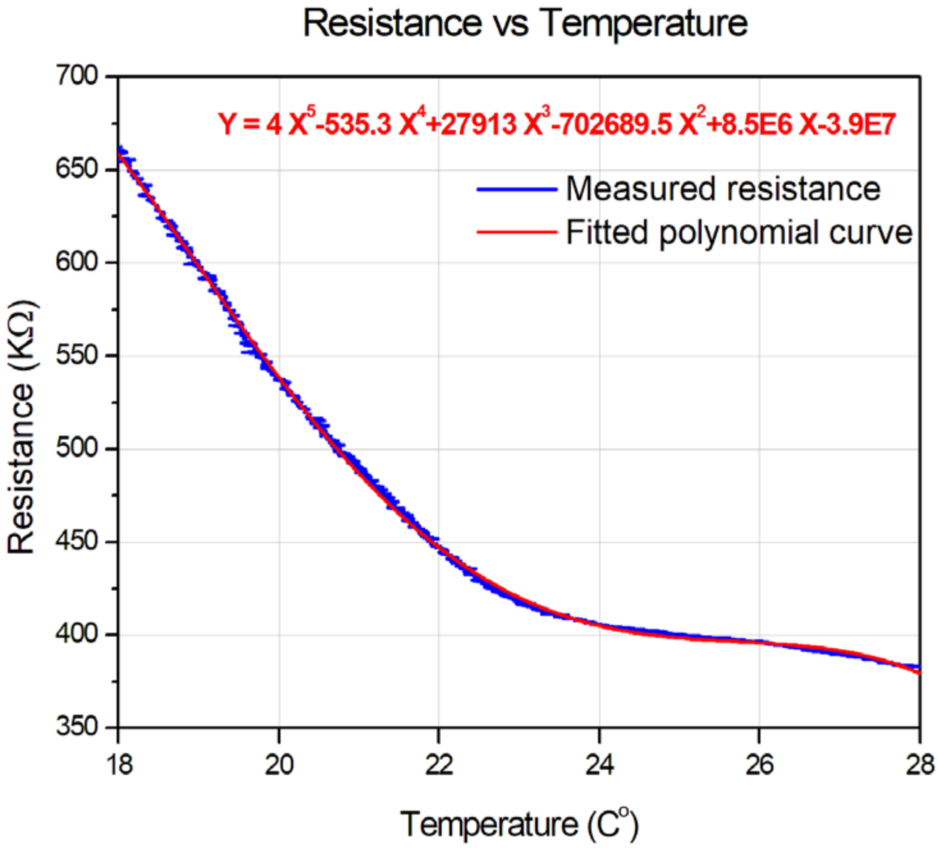

(a)

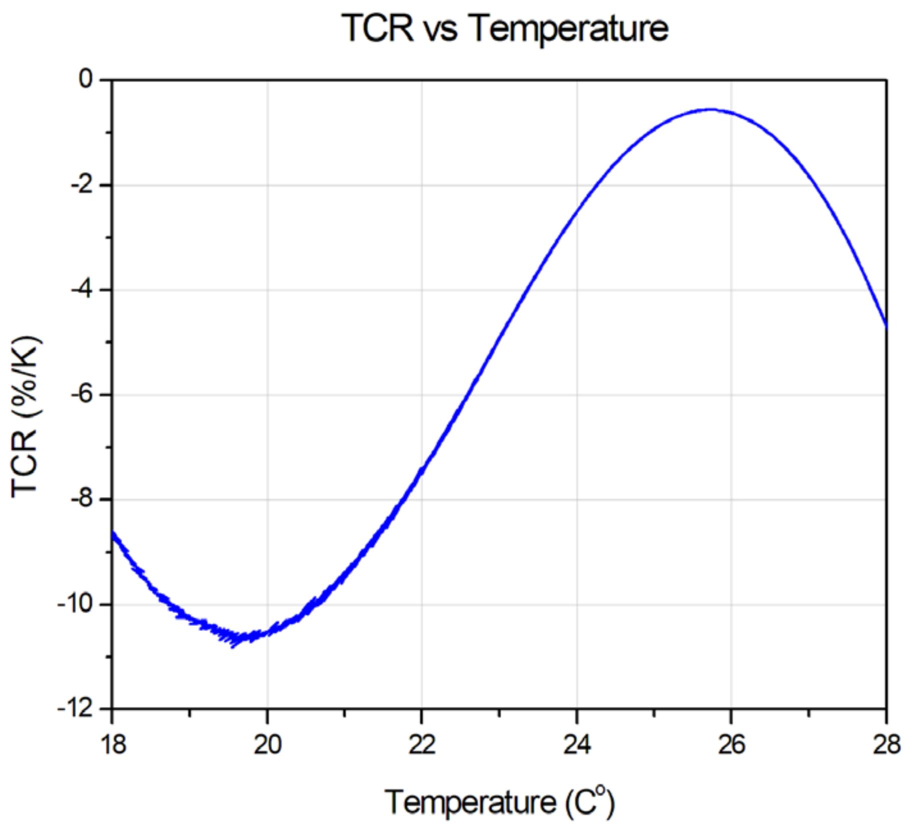

(b)

Figure 4.2. Resistance and TCR variation depending on the temperature. The TCR reaches its maximum value at around 20 °C as -10.5 %/K.

4.2. Noise Measurement

Low noise is another desired property for microbolometer detectors. A resistive element has two major noise components: the thermal noise (Johnson noise) and the 1/f noise (flicker noise). Therefore, only these two components are included and others are neglected in the noise calculations of a resistive microbolometer detector.

The thermal noise originates from the thermal motion of the charge carriers in the thermistor material. It occurs even when any bias is not applied to the resistor (Rogalski, 2011). Although the 1/f noise is accepted as a phenomenon that its reasons are not understood, it shows up at the low frequencies up to several kilohertz (Daniels, 2007).

The noise can be expressed in voltage or current form depending on the bias method of the detector. The total noise current can be described by,

$$i_{Tot} = \sqrt{i_{Th}^2 + i_{1/f}^2} \tag{4.1}$$

where i_{Th} and $i_{1/f}$ represent the thermal noise current and the 1/f noise current which are calculated as in Equation (4.2) and Equation (4.3), respectively.

$$i_{Th} = \sqrt{\frac{4kT\Delta f}{R}} \tag{4.2}$$

$$i_{1/f} = \sqrt{\frac{n{i_d}^2\Delta f}{f^\beta}} \tag{4.3}$$

where k is the Boltzmann constant, T is the temperature, Δf is the measuring bandwidth, R is the detector resistance, n is the 1/f noise parameter, i_d is the detector current, f is the frequency, and β is a parameter in the range of 0.5-2.

The measurement is conducted by applying a constant current of 5 µA on two ZnO resistor structures which are placed in a box that acts as a Faraday Cage, and taking the noise measurement through a dynamic signal analyzer. The graph of the taken measurements is drawn and fitted on a curve to extract the corner frequency value. The corner frequency is the frequency where the thermal noise equals to the 1/f noise. This parameter specifies the noise performance of the detector system. A low corner frequency means that the detector has a low noise in the specified bandwidth. Figure 4.3 gives the noise power spectral density of a ZnO resistor having 400 KΩ resistance at a temperature of 300 K. At the result of the curve fitting, the corner frequency is extracted as 302.5 Hz.

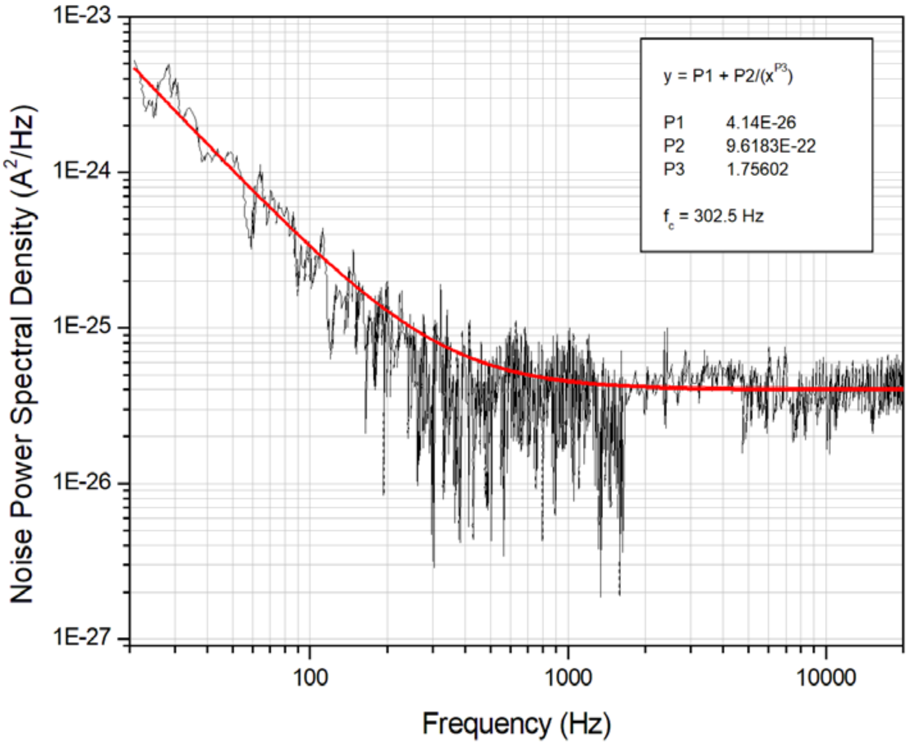

Figure 4.3. The noise power spectral density of a ZnO resistor having 400 KΩ resistance at a temperature of 300 K. The corner frequency is extracted as 302.5 Hz.

4.3. Optical Measurements

The optical measurements are performed by using an FTIR Spectrometer to see the absorption characteristics of the fabricated pixels and compare with the simulated results. The infrared waves in the wavelength range of 2-20 µm are sent on to the fabricated arrays and the amount of the reflected waves from the mirror layer is measured during the measurements. The absorption percentage of the pixel arrays are obtained by taking the difference between the amount of the initially sent waves and the amount of the measured reflected waves.

In the measurements, the arrays from the die #221 are taken as samples. Figure 4.4 shows the combined measurement results of the 7 sample arrays. It is seen that the absorption characteristics of the arrays quite similar to each other, except for the array of A27. A27 is the array which is known its fabrication process is not successfully completed and there is polyimide residue under the middle of the ZnO layer.

A measurement is taken from this pixel array to compare its absorption characteristics with the successfully released pixel arrays and to confirm that the absorption characteristics of the arrays depend on the fabrication success and the other measured pixel arrays are successfully released.

It is observed by the measurements that the average absorption at 8-12 µm wavelength range changes between 30-39 %. It is thought that the reason for this variation is the non-uniformity of the deposited film throughout the wafer. When the measurements are compared with the simulation, it is seen that the measured absorption values are much higher than the simulation which is 9.9 %. The reason for this difference is predicted as the optical properties of the ZnO are affected depending on the temperature in the last step of the fabrication.

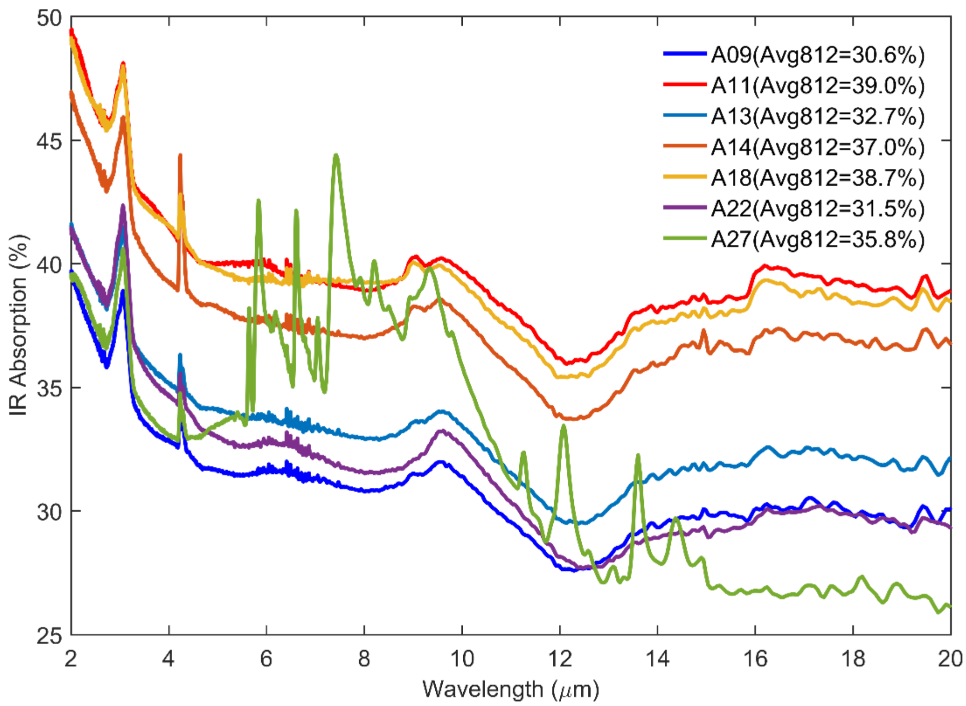

Figure 4.4. Absorption measurements that are taken from various arrays of the die #221.

4.4. Conclusions

The TCR, noise, and absorption measurement results of the fabricated single layer microbolometer detectors are shared in this chapter. The TCR value of the atomic layer deposited ZnO resistor is extracted as -10.5%/K at 20 °C consistent with the reported value in the literature. This is a great value for a microbolometer thermistor material when compared with the commonly used materials. The corner frequency of the 1/f noise is measured as 302.5 Hz at 5 µA bias current. Lower corner frequency means lower electrical noise for the specified bandwidth. The measured value is lower than the reported value in the literature which is 2 kHz (Battal et al., 2014). The reason for that is using a lower bias current. In the results of the optical measurements, the average infrared absorption of the arrays is measured between 30 and 39 %. The reason for obtaining measured values much higher than the simulation is thought as a change in the optical properties of the ZnO due to the fabrication temperature in the last step.

5. CONCLUSIONS AND FUTURE WORKS

In the scope of this research, constructing a single layer structure by using the same material as active layer, absorber, and the structural layer is investigated. The design and development of a single layer microbolometer detector pixel are performed. A single layer microbolometer detector pixel by using atomic layer deposited ZnO is fabricated for the first time in the literature.

The works that are completed in the content of this research can be summarized as below:

1. The performance parameters of a single layer microbolometer detector pixel are specified. 2 types of pixels are designed depending on their arm lengths as long-armed (Type 1) and short-armed (Type 2) pixels. Their performance parameters are optimized by optical, thermal, and mechanical simulations.

2. A 4-step process is designed for the fabrication of the designed single layer microbolometer pixels. The steps are optimized separately. Due to the process limitations which are detected at the optimization steps, the thickness of the ZnO layer is required to decrease to 25 nm, and the corresponding cavity thickness is optimized by revising the optical simulations to maximize the absorption at 8-12 µm wavelength range. The thermal and the mechanical simulations are also revised to see the effects of the decrease in the thickness of the ZnO layer.

3. The fabrication of the designed pixels is completed after the steps are optimized. The deposition and patterning of the gold as the mirror layer is performed by sputtering and RIE methods, respectively. Then, the polyimide material is spin coated to form the sacrificial layer. The anchor openings are patterned by RIE method. The ZnO layer is coated by ALD at 120 °C on to the sacrificial layer and patterned by RIE. Finally, the sacrificial layer is removed by oxygen plasma and pixels are successfully released.

4. The TCR, the noise, and the optical measurements are performed to characterize the fabricated structures. The TCR of the ZnO resistors is obtained as -10.5 %/K at around 20 °C. The corner frequency of the 1/f noise is extracted as 302.5 Hz with a bias current of 5 µA. The average infrared absorption in the wavelength range of 8-12 µm is measured between 30 and 39 %.

Albeit the efforts are exerted to develop the single layer microbolometer detector pixels that have maximum performance, there are still some issues to overcome. Therefore, the future works to have single layer pixels that have better performance can be summarized as follows:

1. The ways to achieve the fabrication of the single layer microbolometer detector pixels with a thicker ZnO layer should be investigated. The arrays that have better absorptance and higher mechanical strength will be obtained by overcoming this issue.

2. The thermal conductance and the responsivity measurements are required to be performed to complete the characterization of the pixels. These measurements could not be performed in the framework of this research since the resistances of the pixels are too high to be measured with the possessed instruments. Being able to fabricate pixels with a thicker ZnO layer can also solve this issue.

3. The reason for the change in the optical properties of the ZnO at the last step of the fabrication should be analyzed and pixel designs should be revised accordingly.

4. As an alternative to increasing the thickness of ZnO layer, a second ZnO layer can be deposited on the first layer in form of a bilayer structure (Poyraz, Gorgulu, Sisman, Tanrikulu, & Okyay, 2017).

5. The single layer pixel structure can be applied to various pixel geometries such as hexagonal geometry which can be more appropriate for the flexible substrates to increase the field of view (Yildizak & Tanrikulu, 2017).

REFERENCES

Ajmera, S. K., Syllaios, A. J., Tyber, G. S., Taylor, M. F., & Hollingsworth, R. E. (2010). Amorphous silicon thin-films for uncooled infrared microbolometer sensors. *Proc. of SPIE, Infrared Technology and Applications XXXVI*, *7660*, 766012. https://doi.org/10.1117/12.850545

Ambrosio, R., Moreno, M., Mireles, J., Torres, A., Kosarev, A., & Heredia, A. (2010). An overview of uncooled infrared sensors technology based on amorphous silicon and silicon germanium alloys. *Physica Status Solidi (C) Current Topics in Solid State Physics*, *7*(3–4), 1180–1183. https://doi.org/10.1002/pssc.200982781

Atar, F. B., Yesilyurt, A., Onbasli, M. C., Hanoglu, O., & Okyay, A. K. (2011). Ge/SiGe quantum well P-I-N structures for uncooled infrared bolometers. *IEEE Electron Device Letters*, *32*(11), 1567–1569. https://doi.org/10.1109/LED.2011.2164390

Awad, E. S., Al-Khalli, N. F., Abdel-Rahman, M. R., Debbar, N. A., & Alduraibi, M. A. (2015). Design and optimization of microbolometer multilayer optical cavity. *Acta Physica Polonica A*, *127*(4), 1295–1297. https://doi.org/10.12693/APhysPolA.127.1295

Awad, Ehab S., Al-Khalli, N., Abdel-Rahman, M., Alduraibi, M., & Debbar, N. (2015). Comparison of V2O5 microbolometer optical performance using NiCr and Ti thin-films. *IEEE Photonics Technology Letters*, *27*(5), 462–465. https://doi.org/10.1109/LPT.2014.2377203

Bagolini, A., Pakula, L., Scholtes, T. L. M., Pham, H. T. M., French, P. J., & Sarro, P. M. (2002). Polyimide sacrificial layer and novel materials for post-processing surface micromachining. *Journal of Micromechanics and Microengineering*, *12*(4), 385–389. https://doi.org/10.1088/0960-1317/12/4/306

Battal, E., Bolat, S., Tanrikulu, M. Y., Okyay, A. K., & Akin, T. (2014). Atomic-layer-deposited zinc oxide as tunable uncooled infrared microbolometer material. *Physica Status Solidi (A) Applications and Materials Science*, *211*(11), 2475–2482. https://doi.org/10.1002/pssa.201431195

Bhan, R. K., Saxena, R. S., Jalwania, C. R., & Lomash, S. K. (2009). Uncooled infrared microbolometer arrays and their characterisation techniques. *Defence Science Journal*, *59*(6), 580–589.

Boreman, G. (2016). *Fundamentals of Infrared and Visible Detector Operation and Testing*. *Wiley* (2nd Ed.).

Bosman, H., Lau, Y. Y., & Gilgenbach, R. M. (2003). Microwave absorption on a thin film. *Applied Physics Letters*, *82*(9), 1353–1355.

Brand, O., & Fedder, G. K. (2005). *CMOS-MEMS: Advanced micro and nanosystems*. *Wiley* (Vol. 2).

Cheng, Q., Paradis, S., Bui, T., & Almasri, M. (2009). Design of a dual-band uncooled infrared microbolometer. *IEEE, Sensors Journal*, *11*(1), 267–277.

Daniels, A. (2007). *Field Guide to Infrared Systems, Detectors, and FPAs*. *SPIE Press* (2nd Ed.).

David, W. B. (2006). *Field Guide to Spectroscopy*. *SPIE Press*.

Dong, L., Yue, R., & Liu, L. (2003). An uncooled microbolometer infrared detector based on poly-SiGe thermistor. *Sensors and Actuators, A: Physical*, *105*(3), 286–292.

Eriksson, P., Andersson, J. Y., & Stemme, G. (1997). Thermal characterization of surface-micromachined silicon nitride membranes for thermal infrared detectors. *Journal of Microelectromechanical Systems*, *6*(1), 55–61.

Erturk, O., Battal, E., Kucuk, S. E., Okyay, A. K., & Akin, T. (2013). A plasmonically enhanced pixel structure for uncooled microbolometer detectors. In *Proc. of SPIE, Infrared Technology and Applications XXXIX* (Vol. 8704, p. 87041E).

Escriba, C., Campo, E., Estève, D., & Fourniols, J. Y. (2005). Complete analytical modeling and analysis of micromachined thermoelectric uncooled IR sensors. *Sensors and Actuators, A: Physical*, *120*(1), 267–276.

Gaussorgues, G. (1994). *Infrared Thermography*. *Springer*.

Graf, A., Arndt, M., Sauer, M., & Gerlach, G. (2007). Review of micromachined thermopiles for infrared detection. *Measurement Science and Technology*, *18*(7). https://doi.org/10.1088/0957-0233/18/7/R01

Henini, M., & Razeghi, M. (2002). *Handbook of Infrared Detection Technologies*. *Elsevier*.

Holst, G. C. (2000). *Common Sense Approach to Thermal Imaging*. *SPIE Press*.

http://www.flirmedia.com/MMC/CVS/Tech_Notes/TN_0005_EN.pdf. (2019).

https://en.wikipedia.org/wiki/Infrared. (2019).

Ichihara, T., Watabe, Y., Honda, Y., & Aizawa, K. (1997). A high performance amorphous Si1-x Cx:H thermistor bolometer based on micro-machined structure. In *Proc. of IEEE, Transducers* (pp. 1253–1256).

Jahanzeb, A., Travers, C. M., Çelik-Butler, Z., Butler, D. P., & Tan, S. G. (1997). A semiconductor YBaCuO microbolometer for room temperature IR imaging. *IEEE Transactions on Electron Devices*, *44*(10), 1795–1801.

Kebapci, B., Dervisoglu, O., Battal, E., Okyay, A. K., & Akin, T. (2014). Broadband absorption enhancement in an uncooled microbolometer infrared detector. *Infrared Technology and Applications XL*, *9070*, 907021.

Kesim, Y. E., Battal, E., Tanrıkulu, M. Y., & Okyay, A. K. (2014). An all-ZnO microbolometer for infrared imaging. *Elsevier, Infrared Physics and Technology*, *67*, 245–249.

Kimata, M. (2018). Uncooled infrared focal plane arrays. *IEEJ Transactions on Electrical and Electronic Engineering*, *13*(1), 4–12.

Kinch, M. A. (2007). *Fundamentals of Infrared Detector Materials*. *SPIE Press*.

Kruse, P. W. (2001). *Uncooled Thermal Imaging Arrays, Systems, and Applications*. *SPIE Press*.

Kruse, P. W., & Skatrud, D. D. (1997). *Uncooled Infrared Imaging Arrays and Systems*. *Semiconductors and Semimetals* (Vol. 47).

Lei, C., Mao, H., Ou, W., Xue, C., Tang, L., Yang, T., … Xiong, J. (2016). A CMOS-MEMS IR device based on double-layer thermocouples. *Microsystem Technologies*, *22*(5), 1163–1171.

Li, C., Skidmore, G., Howard, C., Clarke, E., & Han, C. J. (2009). Advancement in 17-micron pixel pitch uncooled focal plane arrays. *Infrared Technology and Applications XXXV*, *7298*, 72980S.

Liang, H. (2014). Mid-infrared response of reduced graphene oxide and its high-temperature coefficient of resistance. *AIP Advances*, *4*(107131), 1–9.

Lloyd, J. M. (1975). *Thermal Imaging Systems*. *Springer*.

Niklaus, F., Decharat, A., Jansson, C., & Stemme, G. (2008). Performance model for uncooled infrared bolometer arrays and performance predictions of bolometers operating at atmospheric pressure. *Elsevier, Infrared Physics and Technology*, *51*(3), 168–177.

Niklaus, F., Vieider, C., & Jakobsen, H. (2007). MEMS-based uncooled infrared bolometer arrays: a review. In *MEMS/MOEMS Technologies and Applications III* (Vol. 6836, p. 68360D).

P.W.Kruse. (1999). Uncooled IR focal plane arrays. *Opto-Electronics Review*, *7*(4), 253–258.

Perera, A. G. U. (2012). *Bolometers*. *Intech*.

Piotrowski, J., & Rogalski, A. (2007). *High-Operating-Temperature Infrared Photodetectors*. *SPIE Press*.

Poyraz, M., Gorgulu, K., Sisman, Z., Tanrikulu, M. Y., & Okyay, A. K. (2017). LWIR all-atomic layer deposition ZnO bilayer microbolometer for thermal imaging. *Optical Engineering*, *56*(3), 037106.

Pozar, D. M. (2012). *Microwave Engineering*. *Wiley* (4th Ed.).

Rogalski, A. (2003). Infrared detectors: Status and trends. *Progress in Quantum Electronics*, *27*(2–3), 59–210.

Rogalski, A. (2011). *Infrared Detectors*. *CRC Press* (2nd Ed.).

Ryzhii, V., Otsuji, T., Ryzhii, M., Ryabova, N., Yurchenko, S. O., Mitin, V., & Shur, M. S. (2013). Graphene terahertz uncooled bolometers. *Journal of Physics D: Applied Physics*, *46*(065102).

Saxena, R. S., Bhan, R. K., Jalwania, C. R., & Khurana, K. (2008). Effect of excessive bias heating on a titanium microbolometer infrared detector. *IEEE Sensors Journal*, *8*(11), 1801–1804.

Saxena, Raghvendra Sahai, Bhan, R. K., Rana, P. S., Vishwakarma, A. K., Aggarwal, A., Khurana, K., & Gupta, S. (2011). Study of performance degradation in Titanium microbolometer IR detectors due to elevated heating. *Infrared Physics and Technology*, *54*(4), 343–352.

Senveli, S. U. (2010). *Development of High Thermal Performance Uncooled Infrared Detector Pixels With Enhanced Resistor Structures*. M.Sc Thesis, Electrical and Electronics Engineering Department, Middle East Technical University.

Shie, J., Chen, Y., Ou-yang, M., & C. S. Bruce. (1996). Characterization and Modeling of Metal-Film Microbolometer. *IEEE, Journal of Microelectromechanical Systems*, *5*(4), 298–306.

Syllaios, A. J., Schimert, T. R., Gooch, R. W., McCardel, W. L., Ritchey, B. A., & Tregilgas, J. H. (2000). Amorphous Silicon Microbolometer Technology.

Materials Research Society, *609*, 1–6.

Tanrikulu, M. Y., Civitci, F., & Akin, T. (2008). A new method to estimate the absorption coefficient for uncooled infrared detectors. In *Proc. of SPIE, Infrared Technology and Applications XXXIV* (Vol. 6940, p. 694027).

Tanrikulu, M. Yusuf. (2007). *An Uncooled Infrared Microbolometer Array Using Surface Micromachined MEMS Technology*. Ph.D. Thesis, Electrical and Electronics Engineering Department, Middle East Technical University.

Tanrikulu, M. Yusuf, Yildizak, C., Okyay, A. K., Akar, O., Sarac, A., & Akin, T. (2018). Single layer microbolometer detector pixel using ZnO material. *Proc. of SPIE, Infrared Theory and Applications XLIV*, *10624*, 1062417.

Tiffany, W. B. (1975). Introduction and review of pyroelectric detectors. In *Proc. of SPIE, Infrared Technology* (Vol. 62, pp. 153–158).

Tissot, J. L., Durand, A., Garret, T., Minassian, C., Robert, P., & Tinnes, S. (2010). High-performance uncooled amorphous silicon VGA IRFPA with 17 µm pixel-pitch. In *Proc. of SPIE, Infrared Technology and Applications XXXVI* (Vol. 7660, p. 76600T).

Travers, C. M., Jahanzeb, A., Butler, D. P., & Çelik-Butler, Z. (1997). Fabrication of semiconducting YBaCuO surface-micromachined bolometer arrays. *IEEE, Journal of Microelectromechanical Systems*, *6*(3), 271–276.

Tsutsumi, K., Yamashita, A., & Ohji, H. (2002). The experimental study of high TCR Pt thin films for thermal sensors. *Proc. of IEEE*, 1002–1005.

Voshell, A., Dhar, N., & Rana, M. M. (2017). Materials for microbolometers: vanadium oxide or silicon derivatives. In *Proc. of SPIE, Image Sensing Technologies: Materials, Devices, Systems, and Applications IV* (Vol. 10209, p. 102090M).

Wada, H., Sone, T., Hata, H., Nakaki, Y., Kaneda, O., Ohta, Y., & Ueno, M., and Kimata, M. (2001). YBaCuO uncooled microbolometer IRFPA. *Proc. of SPIE, Infrared Technology and Applications XXVII*, *4369*(5), 297.

Wang, B. (2012). Vanadium oxide microbolometer with gold black absorbing layer. *SPIE Press, Optical Engineering*, *51*(7), 074003.

Wang, B., Lai, J., Li, H., Hu, H., & Chen, S. (2013). Nanostructured vanadium oxide thin film with high TCR at room temperature for microbolometer. *Elsevier, Infrared Physics and Technology*, *57*, 8–13.

Wolfe, W. L. (1996). *Introduction to Infrared System Design*. *SPIE Optical*

Engineering Press.

Wood, R. A. (1995). Use of Vanadium Oxide in Microbolometer Sensors. *US Patent no. 5450053*.

Xu, D., Wang, Y., Xiong, B., & Li, T. (2017). MEMS-based thermoelectric infrared sensors: A review. *Frontiers of Mechanical Engineering*, *12*(4), 557–566.

Yildizak, C., Okyay, A. K., & Tanrikulu, M. Y. (2017). Process Design and Thermal Simulations of a Single Layer Microbolometer. In *Proc. of International Advanced Researches & Engineering Congress* (pp. 1040–1044).

Yildizak, C., & Tanrikulu, M. Y. (2017). Hexagonal microbolometer pixel for flexible substrates. In *Proc. of IEEE, 10th International Conference on Electrical and Electronics Engineering, ELECO* (pp. 2–5).

Yole Développement. (2017). *Uncooled Infrared Imagers, Market & Technology Report*.

Yon, J.-J., Mottin, E., & Tissot, J.-L. (2008). Latest amorphous silicon microbolometer developments at LETI-LIR. In *Proc. of SPIE, Infrared Technology and Applications XXXIV* (Vol. 6940, p. 69401W).

Yoneoka, S., Liger, M., Yama, G., Schuster, R., Purkl, F., Provine, J., Prinz, F. B., Howe, R. T., and Kenny, T. W. (2011). ALD-metal uncooled bolometer. *Proc. of IEEE, International Conference on Micro Electro Mechanical Systems (MEMS)*, 676–679.

CURRICULUM VITAE

Personal Information

Surname, Name	YILDIZAK, Çiğdem
Date of birth	
Place of birth	
Nationality	
Phone	
E-mail	

Education

2017 - 2019	M. Sc. Department of Electrical-Electronics Engineering, Adana Alparslan Türkeş Science and Technology University, Adana, TURKEY
2009 - 2014	B. Sc. Department of Electrical and Electronics Engineering, Hacettepe University, Ankara, TURKEY
2004 - 2008	Adana İncirlik Lisesi (Y.D.A.), Adana, TURKEY

Work Experience

Mar 2017-	*Research and Teaching Assistant*, Department of Electrical-Electronics Engineering, Adana Alparslan Türkeş Science and Technology University, Adana, TURKEY
Feb 2016 - Mar 2017	*Embedded Systems Design Engineer*, DCL Information Management Solutions, Adana, TURKEY
Feb 2015 - Jan 2016	*System Design Engineer*, VESTEL Elektronik A.Ş., Manisa, TURKEY
Aug2013 – Sep 2013	*Intern,* Türk Telekom A.Ş., Ankara, TURKEY

Foreign Languages

English

Hobbies

Chess, Latin Dances, Yoga, Theatre

International Conference Publications

1. Tanrıkulu M. Y., **Yıldızak Ç.**, Okyay A. K., Akar O., Saraç A., and Akın T., "Single layer microbolometer detector pixel using ZnO material," *Proc. of SPIE, Infrared Technology and Applications XLIV*, Vol. 10624, p. 1062417, 2018.

2. **Yıldızak Ç.**, Tanrıkulu M. Y. "Hexagonal microbolometer pixel for flexible substrates," *10th International Conference on Electrical and Electronics Engineering (ELECO)*, p. 2-5, 2017.

3. **Yıldızak Ç.**, Okyay A. K., Tanrıkulu M. Y. "Process design and thermal simulations of a single layer microbolometer," *International Advanced Researches and Engineering (IAREC)*, p.1040-1044, 2017.